ISSN 1028-8546

Volume XXIX Number 3
Section: En October 2023

Azerbaijan Journal of Physics

Fizika

www.physics.gov.az
www.physics.gov.az/ajpfizika.html

Institute of Physics
Ministry of Science and Education Republic of Azerbaijan

Published from 1995
Ministry of Press and Information
of Azerbaijan Republic,
Registration number 514, 20.02.1995

ISSN 1028-8546
vol. XXIX, Number 03, 2023
Section: En

Azerbaijan Journal of Physics

FIZIKA

Ministry of Science and Education Republic of Azerbaijan
Institute of Physics

PUBLISHING OFFICE

131, H. Javid ave., AZ-1143, Baku
Ministry of Science and Education Republic of Azerbaijan
Institute of Physics

Tel.: (99412) 539-51-63, 539-32-23
Fax: (99412) 537-22-92
E-mail: jophphysics@gmail.com
Internet: www.physics.gov.az

It is authorized for printing:

INFLUENCE OF DOPING BY Zn (0.01 at% Zn) ON CONDUCTIVITY OF InGaSb EQUIMOLAR COMPOSITION

S.Z. DAMIROVA, V.I. EMINOVA
Institute of Physics of Ministry of Science and Education of Azerbaijan Republic,
H.Javid ave., 131, Az-1143, Baku, Azerbaijan
suzanna_ismailova@mail.ru, vusaleeminova84@gmail.com

The investigations of Hall coefficient and thermo-e.m.f. in $In_{0,5}Ga_{0,5}Sb$ doped by Zn (up to 0.01 at% Zn) in temperature interval T=100-500 K are carried out. It is revealed that the highly mobile electrons make the significant contribution into Hall coefficient in equimolar composition at T>350 K. It is established that the contribution of highly mobile electrons is suppressed in $In_{0,5}Ga_{0,5}Sb$ equimolar composition with increase of Zn content and the conductivity has the hole character. The effective mass of holes ($m^*=0.36m_0$) is evaluated by data of thermo-e.m.f.

Keywords: $In_{0,5}Ga_{0,5}Sb$, Hall coefficient, thermo-e.m.f.
PACS: 64.75.Nx; 72.20.Pa

INTRODUCTION

InSb-GaSb solid solutions pay attention of investigators by their well solubility of initial binary compounds up to $In_{0,5}Ga_{0,5}Sb$ equimolar composition. The low values of thermal conduction and carrier effective mass [1 – 3] in this system allow us to recommend this object for the formation of different recorders: thermal receptor, Hall probes and etc. [4–6].

The doping of $In_{0,5}Ga_{0,5}Sb$ equimolar composition allows us to vary the crystal parameters.

The investigation results of the influence of Zn atom introduction (0.001 at% Zn and 0.01 at % Zn) in initial matrix of equimolar composition on concentration and thermo-e.m.f. S are presented in this work. This allows us to predict the direction of increasing of recorder characteristics.

EXPERIMENTAL PART

The large-block polycrystalline samples are obtained by the method of direct alloying of initial materials In(99.000%), Ga(99.999%) Sb (0000) and Zn (pure for synthesis).

The ampoule heating with the given substances is carried out up to 700^0C. The zone leveling with the consistency of molten zone passage, width 3-4 mm with velocity 5.2 and 1 mm/h at temperature 700^0C is carried out. The samples in the form of parallelepipeds $12\times5.2\times2.5mm^3$ are cut from obtained ingots. The measurements of Hall coefficient R and thermo-e.m.f. S are carried out by four-probe potentiometric method in temperature interval T=100-500 K.

The temperature dependences of Hall coefficient R for equimolar $In_{0,5}Ga_{0,5}Sb$ (1) and doping of Zn: $In_{0,5}Ga_{0,5}Sb$ +0.001at% Zn(2), $In_{0,5}Ga_{0,5}Sb$ +0.01at% Zn (3) are shown in Fig.1.

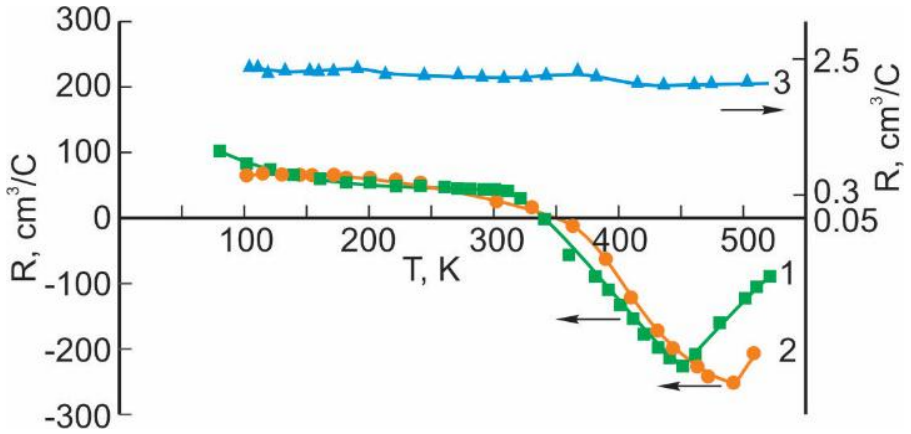

Fig. 1. Temperature dependences of Hall coefficients in $In_{0,5}Ga_{0,5}Sb$ (1), $In_{0,5}Ga_{0,5}Sb$ +0.001ат% Zn (2), $In_{0,5}Ga_{0,5}Sb$ +0.01ат%Zn (3).

As it is seen Hall coefficient in initial equimolar composition (sample 1) in temperature interval T=100-300 K weakly changes with temperature, further, at T≈350K changes the sign on the negative one. Further, the temperature dependence R(T) passes through the maximum at T≈440K. Such behavior can be explained by the following way. At T<300 K the conductivity is carried out by the holes. The ionization of deep donor is carried at T>300K by that the sign inversion R(T) and the further increase of Hall coefficient is caused. The passing of R(T) dependence through the maximum is caused by competitive

131, H.Javid ave, AZ-1143, Baku
Institute of Physics
E-mail: jophphysics@gmail.com

contribution in the conductivity of the holes and electrons and further, by predominating of electron conductivity.

The character of temperature dependence R(T) practically doesn't change at introduction 0.001a%Zn (sample 2). The further increase of Zn (0.001at%Zn-sample 3) content leads to the decrease on approximately value order of Hall coefficient. As it is seen R>0 for this composition in whole investigated interval. One can predict that increase of Zn atom content leads to significant increase of active impurity centers and moreover, to significant compensation of electron contribution into Hall effect.

The temperature dependences of S thermo-e.m.f. shown in Fig.2 is the proof of these preliminary conclusions.

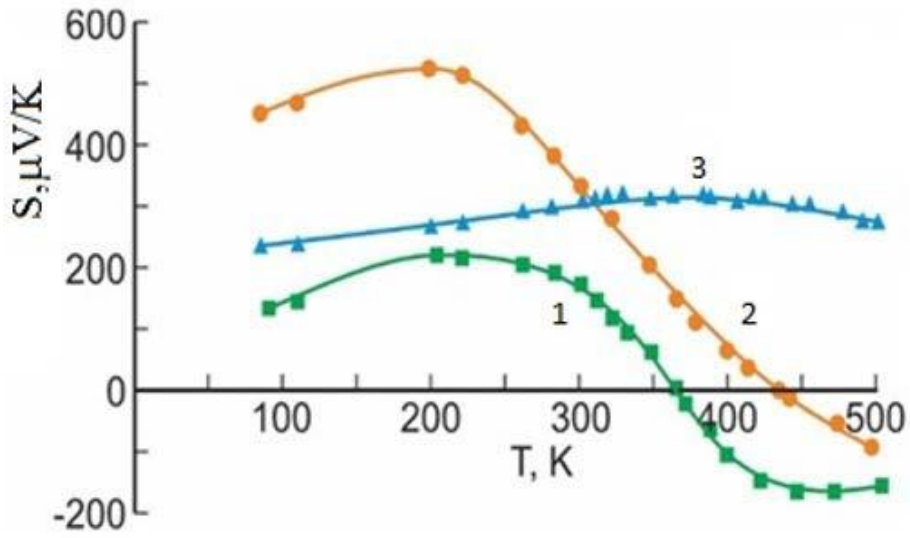

Fig. 2. Temperature dependences of thermo-e.m.f. of $In_{0,5}Ga_{0,5}Sb$ (1), $In_{0,5}Ga_{0,5}Sb$ +0.001at% Zn (2), $In_{0,5}Ga_{0,5}Sb$ +0.01at%Zn (3).

The dependence of thermo-e.m.f. on temperature S(T) in equimolar composition $In_{0,5}Ga_{0,5}Sb$ (sample 1) is like the dependence of Hall coefficient R(T): up to T≤360 K, thermo-e.m.f. is positive one; further the inversion of α_0 sign on negative one and later increase of thermo-e.m.f. S with temperature takes place. The small increase of S thermo-e.m.f. in interval from 100K up to 200K is caused by mixed character of scattering carriers on impurity ions and acoustic phonons. The decrease of S thermo-e.m.f. value in temperature interval from 200K up to sign inversion point is caused by the beginning of the ionization of donor centers and increase of the contribution of more mobile electrons in total thermo-e.m.f. S. This also explains S(T) increase in the region where S<0. The doping of the initial composition 0.001 at % Zn (sample 2) leads to the thermo-e.m.f. S more than in 2 times, the inversion point of thermo-e.m.f. S sign shifts to the side of more high temperatures (T≈430K). Such behavior of S(T) for $In_{0,5}Ga_{0,5}Sb$+0.001at% Zn sample evidences on the fact that the doping by Zn leads to the increase of acceptor center number. The temperature dependence of thermo-e.m.f. S(T) in $In_{0,5}Ga_{0,5}Sb$+0.01at% Zn (sample 3) evidences on total suppression of electron contribution in thermo-e.m.f. S.

DISCUSSION

The weak dependence of Hall coefficient R(T) on temperature in temperature interval 100 – 300K in $In_{0,5}Ga_{0,5}Sb$ and $In_{0,5}Ga_{0,5}Sb$ +0.001at% Zn samples (see Fig.1) allows us to evaluate the hole concentration.

№ of the sample	Composition	p ,cm^{-3}
1	$In_{0,5}Ga_{0,5}Sb$	$4.4 \cdot 10^{16}$
2	$In_{0,5}Ga_{0,5}Sb$ +0.001at% Zn	$3 \cdot 10^{17}$
3	$In_{0,5}Ga_{0,5}Sb$ +0.01at% Zn	$2.9 \cdot 10^{18}$

The same evaluation of hole concentration by the data of temperature dependence of Hall coefficient R(T) in the whole investigated temperature interval 100 – 500K (where R on T practically doesn't depend) gives the value $\rho=2.9 \cdot 10^{18}$ cm $^{-3}$ (see Fig. 1). The increase of hole concentration with increase of Zn content evidences on the fact that the doping of Zn atoms leads to formation of additional electroactive centers.

If we take under the consideration the fact that hole scattering on acoustic phonons dominates in temperature interval 200 – 300K, so by the known ratio [6]:

$$S = \frac{k_0}{e}\left[\frac{F_{r+2(\eta^*)}}{F_{r+1(\eta^*)}} - \eta^*\right], \qquad (1)$$

(where $F_r(\eta*)$ is Fermi one-parameter integral, $\eta* = \eta/k_0T$ is given chemical potential, r is parameter of scattering mechanism of charge carriers, at scattering on acoustic phonons r=0) one can estimate the given chemical potential.

One can estimate the hole effective mass by the data of concentration and given chemical potential by the formula [7]:

$$\rho = \frac{(2m_p k_0 T)}{3\pi^2\hbar^3} F_{3/2}\ (\eta^*) \quad , \qquad (2)$$

The value of hole effective masses are practically similar and equal to $m_p^* = 0.36m_0$ for the investigated compositions.

CONCLUSION

Thus, the analysis of the obtained results shows that the introduction of Zn up to 0.01at % in $In_{0,5}Ga_{0,5}Sb$ equimolar composition leads to the formation of impurity centers of acceptor type, as a result of which the conductivity has the pure hole character. The effective mass of the holes $m_p^* = 0.36m_0$ is estimated on the base of data of thermo-e.m.f.

[1] *V.N. Kumar, Y. Hayakawa, H. Udono and Y. Inatomi.* An Approach to optimize the thermoelectric properties of III-V ternary InGaSb crystals an microscale composional segretations. İnorqganik Chemistry, Stokholm 2019.

[2] *N. Kumar, V. Arivanandan, M. Koyoma, T. Udono, H. İnatomi, Y. Hayakawa*. Effects of varying Indium Compozitions on the Thermoelectric properties of $In_xGa_{1-x}Sb$ ternary alloys. Appl.Phys. A.Mater.Sci.Process 2016, 122.885.

[3] *S.A. Zeynalov, S.A. Aliyev*. Turk. J.Phys, 20(5) 477, 1996.

[4] *D.S. Abramkin, V.V. Afuchin.* Novel InGaSb /AlP Quantum Dots for Non- volatile memories. Nanomaterials 2022, 12, 3794-3814.

[5] *Z. Du, M. Yan, & J. Zhu.* Thermoelectric performance of $In_{0.8}+yGa_{0.2}Sb$ ($0 \leq y \leq 0.06$) ternary solid solutions with In excess. Materials Research Express. 2018.

[6] *P.I. Baranskiy, V.B. Klochokov, I.V Potikevich.* Semiconductor electronics, Kiev 1975.

[7] *B.A. Askerov.* Electronic transport phenomena in semiconductors. Science 1985.

Received: 16.05.2023

STRUCTURAL ORIGIN OF SILK NANOPARTICLES AND THEIR STABILIZATION

A.M. MAMMEDZADE, B.U. GASIMLI
Institute of Biophysics, Ministry of Science and Education Republic of Azerbaijan
Z. Khalilov, 117, Baku, AZ 1171
E-mail: mesimlia@mail.ru;basira.qasimli.usubali@bsu.edu.az

A naturally occurring biopolymer known as silk fibroin (SF) has several distinctive qualities that make it an ideal vehicle for the delivery of drugs and a variety of therapeutic agents. It has been demonstrated that drugs and biomolecules can be successfully delivered via SF matrices. In this study homogenous SF nanoparticles (SFNP) obtained with a size ranging between 171-207 nm. SFNPs were stabilized with GA (glutaraldehyde) which is known as a cross-linking agent was used to stabilize the SFNPs. The stabilized SFNPs were consistent for 4 days. Circular dichroism (CD) and Fourier-transform infrared spectroscopy (FTIR) studies revealed random-coil to beta structure transition with beta structure reaching up to 59 %. Observed birefringence of Congo red staining in a polarized microscope indicates beta amyloid formation. Thus, SFNPs composed of amyloid nanoparticles.

Keywords: silk fibroin, silk nanoparticles, cross linker, amyloids.
PACS: 87.64.−t; 87.64.Cc

1. INTRODUCTION

Silk fibroin is a natural biomaterial with important biological and mechanical properties. SF retains a superb blend of mechanical and biological characteristics that are difficult to find together in other natural or synthetic materials, and which are mainly determined by its secondary structure. It is one of the toughest biomaterials found in nature, with toughness higher than Kevlar (a para-aramid synthetic fiber used to make bulletproof vests), showing high tensile strength, stiffness and remarkable stability, especially when processed at high temperatures (above 250°C), without altering its stability and structure [1]. As compared to other silks from the silkworm family, B. mori SF has the highest tensile strength and modulus.

There are numerous and inexpensive sources of this natural polymer because silkworms are widely cultivated for the textile industry. The raw cocoon filaments are made up of fibroin (75%) and sericin proteins (25%) where two parallel fibroin fibers are bound together by a coating of sericin proteins [2-4]. For medical applications, the sericin component must be properly removed so the fibroin fibers can be further processed into various materials [5].

Nowadays, the use of nanoparticles to deliver small molecules is rapidly growing in many fields. The unique properties of nanoparticles could overcome the limitations of using small molecules as therapeutic agents in biomedical applications. The fabrication of silk nanospheres is a more challenging area of research than the fabrication of silk microspheres because of the high molecular weight and protein nature of silk [6]. Many different techniques are used to produce nanoparticles from regenerated SF by taking advantage of the hydrophilic and hydrophobic chain interactions that govern silk's ability to self-assemble. In this study we used dehydration method to produce silk nanoparticles which then treated with glutaraldehyde (GA) as the cross-linking agent to stabilize SF nanoparticles. Crosslinking rigidifies and deactivates many biological functions, so in this way, glutaraldehyde solutions are used as biocides and as fixative [7]. Among the many protein crosslinking substances on the market, GA has unquestionably found the broadest use in a variety of industries, including biomedical and pharmaceutical sciences, histochemistry, microscopy, cytochemistry, the leather tanning industry, enzyme technology, and chemical sterilization. A clear, colourless to pale straw-coloured, fragrant oily liquid, GA is a linear, 5-carbon dialdehyde that is soluble in all quantities in water, alcohol, and organic solvents. It is mostly offered as acidic aqueous solutions with a pH range of 3.0-4.0, with concentrations ranging from less than 2% to 70% (w/v).

The results provided here reveals, that GA can stabilize the silk nanoparticles for several days without any aggregation which prolongs the life of silk nanoparticles by reducing the cost of production. For medical purposes it could increase the storage time and target particles for drug delivery. Using acetone as dehydrating agent we fabricated silk nanoparticles of 171-207 nm size. SFNPs treated with glutaraldehyde (GA) are able to preserve their stability up to 4 days in a row. Results from CD and FTIR concluded a transformation from random coil to beta structure to 59%. Amyloid formation was verified with Congo red staining on a birefringence in a polarized microscope.

2. EXPERIMENTAL SECTION

2.1 Sample preparation

A commonly used method was applied to extract SF from the silk cocoons made by B. mori silkworms [8]. To remove sericin, silk cocoons were cut into small pieces and cooked for 30 minutes in 0.02 M Na_2CO_3 (Fisher Science). The resulting SF was dissolved in 10.5 M LiBr solution (Sigma-Aldrich) at

131, H.Javid ave, AZ-1143, Baku
Institute of Physics
E-mail: jophphysics@gmail.com

60ºC for 4 hours and dialyzed against deionized water at 4ºC for 43 hours. After dialysis, the final concentration of SF was between 23 and 27 mg/mL. UV measurements of the SF concentration were made using the formula ε^{275nm}= 1.064 cm-1(mg/mL)$^{-1}$ [9] and MW = 390 kDa.

SF solution was added to acetone dropwise and at the end of the experiment the concentration of acetone was not below 70%.

GA was purchased from Sigma-Aldrich. GA was dissolved in water to obtain with 8% glutaraldehyde solution [9] which was then added into treated SF and kept on magnetic stirrer for 12 hours at a room temperature. Then SFNPs were extracted from the solution via centrifugation.

2.2 Circular dichroism spectroscopy

Circular dichroism spectra were measured on a Chirascan V100 (Applied Photophysics, UK) at room temperature under constant nitrogen flush over a wavelength range of 180-260 nm using step size of 0.5 nm and bandwidth of 1 nm. The quartz cuvette with path length of 0.2 mm was used for the measurements. Chirascan V100 is equipped with a solid state Large Area Avalanche Photodiode (LAAPD) detector, allowing good signal detection at 180 nm.

2.3 Fourier-transform infrared spectroscopy

Infrared absorption spectra were recorded with a Vertex 70 FTIR spectrometer (Bruker Optics, Ettlingen, Germany). FTIR is a useful tool to monitor SF structural changes in various conditions. Protein materials are characterized by the position and intensity of the amide I, amide II, and amide III bands. However, Amide I band was used to calculate the secondary structure of the protein. Amide I band of the proteins were fit to Gaussian components using Origin Lab 2016 Software.

2.4 Congo Red binding assay

Congo Red is one of the most widely used amyloid dyes. Because of its extensive β - sheet structure CR binds to amyloid proteins. When a dye binds to amyloid, its absorbance spectrum is changed [10].

The Congo Red (CR) concentration was calculated using the extinction coefficient ε_{490nm} = $3.3x10^4$ [11]. In deionized water, the dye was freshly produced, and samples were adjusted to achieve a final concentration of 20 μM. A Shimadzu UV-2700 spectrophotometer was used to record the mixture's absorption spectra from 400 to 700 nm.

By using a microscope and crossed polarizers, CR staining experiments were carried out to observe the beta-amyloid aggregates of the SF solution. Congo red molecules are oriented on amyloid fibrils, which causes the dye to become birefringent. Amyloid stained by Congo red usually shows apple-green birefringence in cross-polarized light [12].

3. RESULTS AND DISCUSSION

3.1. Particle size and stability analysis

To find out the size of the obtained silk nanoparticles Dynamic light scattering (Zetasizer Nano ZS, Malvern Instruments, Malvern, UK) measurements operating at λ= 633 nm was used 4 days in a row. As shown in the figures below (Figure 1 and 2) the solution of fibroin nanoparticles prepared with acetone showed a single peak with a diameter of 171 nm on the first day following with 188 nm, 207 nm, 189 nm on other days respectively. Silk nanoparticles showed a good stability even after several days without aggregation.

As can be seen in the figure 2 obtained silk nanoparticles are basically homogenous. During 4 days we haven't seen any changes in size of the nanoparticles. On average the size of SFNPs are 189 ±15 nm.

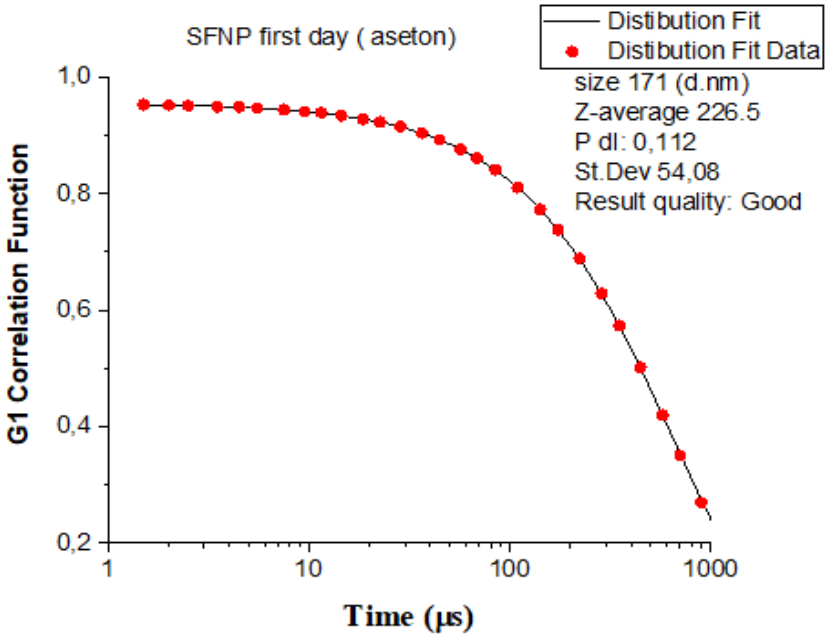

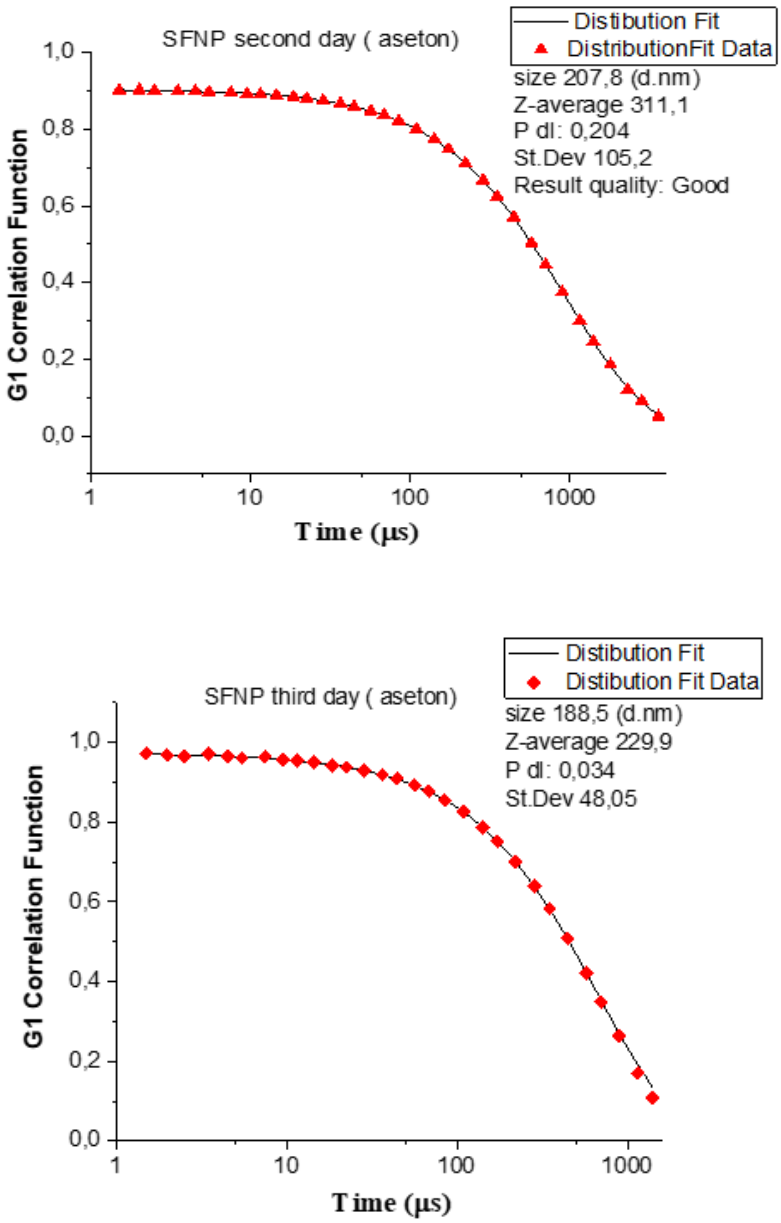

Fig 1. Fitting analysis of SFNPs in Dynamic Light Scattering.

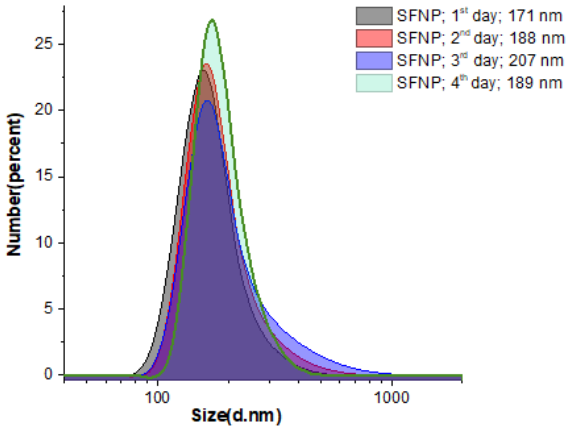

Fig. 2. Size distribution of SFNPs in Dynamic Light Scattering.

3.2. Secondary structure analysis

3.2.1. CD analysis

CD is one of the best measurements to characterize SF in solution. It is a powerful technique to evaluate any conformational changes in the structure of proteins [13]. The secondary structure of SF can be determined by CD spectroscopy in the 'far-UV' spectral region (190–250 nm).

In figure 3, SF solution displayed a single negative band at around 195 nm, characteristic of random coil conformation, whereas SFNP showed a characteristic β-sheet structure with positive peak at 195 nm and negative at 220 nm respectively.

Conformational changes of proteins can be assessed using Fourier-transform infrared spectroscopy (FTIR) as well. Amide I vibrational band is the most sensitive spectral region used to study protein secondary structure. Figure 4 illustrates infrared spectra between 1560-1720 cm^{-1} for SF solution. Amide 1 band of the SF solution estimated secondary structure of the silk. Beta sheet formation was clearly seen under acetone treatment of silk nanoparticles. Assignments of the components shown in Table 1.

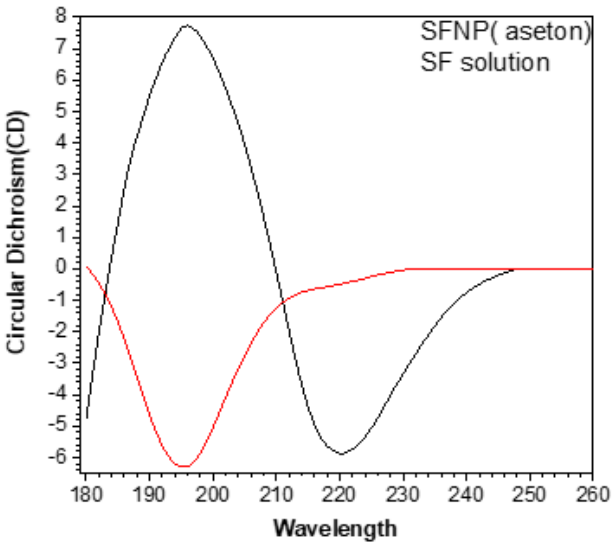

Fig. 3. Far-UV CD spectra of SF. Black and red lines represent SFNP and SF solutions, respectively.

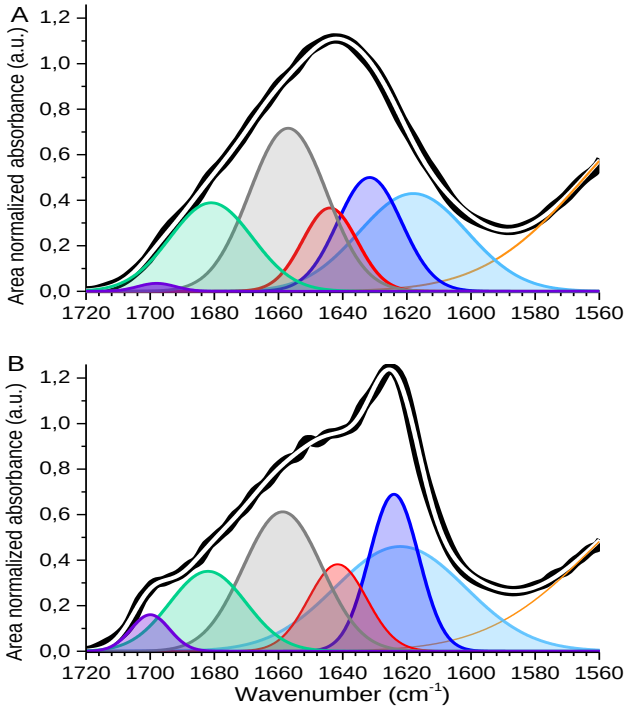

Fig. 4. Infrared spectra of SF.

Table 1.

Estimation of secondary structure elements for various SF films from deconvolution of Amide I bands of FTIR spectra.

	1700cm^{-1} Intermolecular β-sheet (antiparallel)	1683cm^{-1} β-turn	1658cm^{-1} Random coil	1641cm^{-1} α-helix	1622cm^{-1} Intramolecular β-sheet	1615cm^{-1} Intermolecular β-sheet (aggregate)	1622cm^{-1} Side chain	Total β-structure
SF films	0,7	17,2	29,4	10,7	17,1	24,9	0	59.9
SFNP	3,1	13,6	24,2	11,2	17,3	30,5	0	64.5

All data show that we have silk fibroin aggregates, however, not all β-sheet aggregates are amyloids. Therefore, we used Congo Red staining assay to find out whether aggregates are amyloid or not.

Under a cross- polarized microscope, the green birefringence dots were seen in the SFNP solution with CR. According to this finding, attached CR molecules are arranged in an amyloid-like manner, with alignment along the fibre axis. The birefringence is visible in other protein aggregates when bound CR molecules are arranged arbitrarily. In figure 6 amyloid fibrils were seen during birefringence with CR.

It has been shown that CR is dichroic and, as a result, the change in intensity of red can be easy to see in smears of Congo red [14].

UV-VIS spectroscopy was also used to examine the CR-SFNP complex and to show the specific binding of CR with silk fibroin nanoparticles. Upon for the figure 7 increasing concentration of silk fibroin indicates red shift of the absorbance band of Congo Red dye.

As CR binds to SFNP, the resulting CR-SFNP complex changes the absorbance band according to the CR concentration. As concentrations changed, the isosbestic point shifted, leaving only two states of CR: bound and free. There is no intermediary structure in the transition from the random coil to the beta-sheet structure, according to the observed isodichroic point.

Fig. 5. Birefringence image of SFNP-CR complexes.

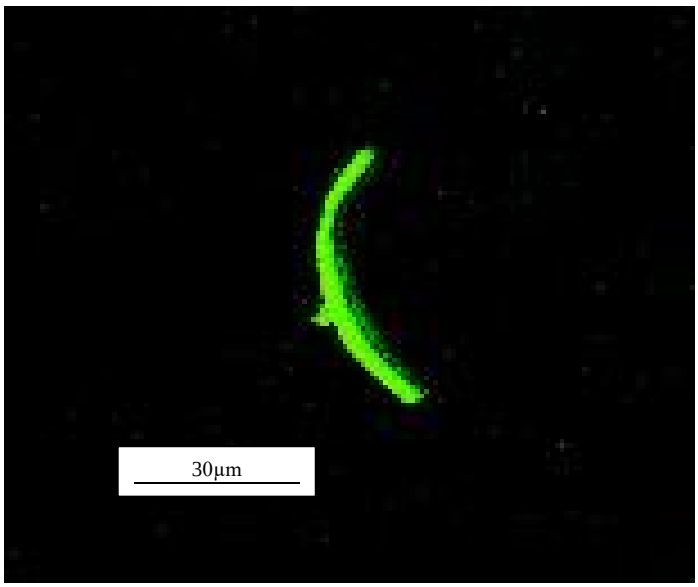

Fig. 6. Birefringence image of SFNP-CR complexes with amyloid fibril.

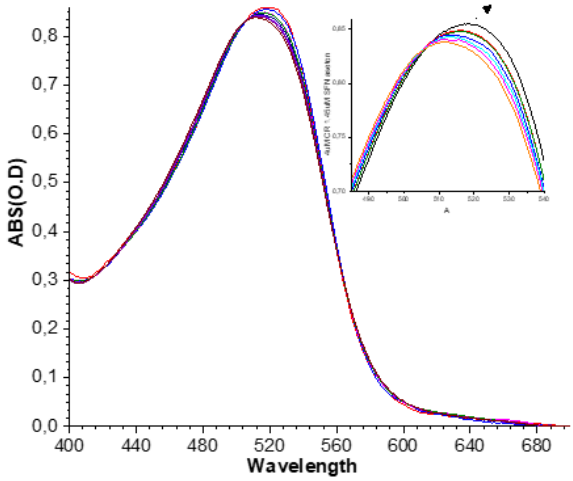

Fig. 7. UV-VIS spectra of CR titrated with increasing concentrations of SF in range of 2 µM- 20 µM.

CONCLUSION

In this research we aimed to achieve the stability of SFNPs by processing them with GA solution. As a result of this procedure, the produced silk nanoparticles showed no signs of clumping even after several days with a constant molecular size of 189±15 nm on average which was ideal for drug delivery and other therapeutic targets. We further presented proof on the basis of CD and FTIR that conformational changes occurred in secondary structure SF nanoparticles where random coil transformed into β-sheet. With CR binding assay we confirmed that β-sheet aggregates were amyloids.

This novel fabrication technique not only increase the productivity of silk-based nanoparticles but also promise to extend the duration of storage for various medical uses.

[1] *B. Crivelli, S. Perteghella, E. Bari, M. Sorrenti, G. Tripodo, T. Chlapanidas, M. Torre.* Silk nanoparticles: from inert supports to bioactive natural carriers for drug delivery. Soft matter, 2018, 14(4), 546–557.

[2] *C.L. Craig.* Evolution of arthropod silks, Annu Rev Entomol 42, 1997, 231-67.

[3] *K. Yamaguchi, Y. Kikuchi, T. Takagi, A. Kikuchi, F. Oyama, K. Shimura, S. Mizuno.* Primary structure of the silk fibroin light chain determined by cDNA sequencing and peptide analysis, J Mol Biol 210(1) (1989) 127-39.

[4] *H. Okamoto, E. Ishikawa, Y. Suzuki.* Structural analysis of sericin genes. Homologies with fibroin gene in the 5' flanking nucleotide sequences, J Biol Chem. 1982, *257(24), 15192-9.*

[5] *D.N. Rockwood, R.C. Preda, T. Yücel, X. Wang, M.L. Lovett, D.L.Kaplan.* Materials fabrication

from Bombyx mori silk fibroin. Nature protocols, 2011, 6(10), 1612–1631.

[6] *F. Mottaghitalab, M. Farokhi, M.A. Shokrgozar, F. Atyabi, H. Hosseinkhani.* Silk fibroin nanoparticle as a novel drug delivery system, Journal of Controlled Release, 2015, (Vol. 206).

[7] *R. Mehravar, M. Jahanshahi, N. Saghatoleslami.* Fabrication and evaluation of Human Serum Albumin (HSA) nanoparticles for drug delivery application. International Journal of Nanoscience, 2009, 8(3).

[8] *W. Huang, S. Ling, C. Li, F.G. Omenetto, D.L. Kaplan.* Silkworm silk-based materials and devices generated using bio-nanotechnology, Chem. Soc. Rev. 2018, 47, *6486–6504.*

[9] *L. Ragona, O. Gasymov, A.J. Guliyeva, R.B. Aslanov, S. Zanzoni, C. Botta, H. Molinari.* Rhodamine binds to silk fibroin and inhibits its self-aggregation, Biochim. Biophys. Acta, Proteins Proteomics, 2018, 1866, 661–667.

[10] *W.E. Klunk, R.F. Jacob, R.P. Mason.* Quantifying amyloid beta-peptide (Abeta) aggregation using the Congo red-Abeta (CR-abeta) spectrophotometric assay. Anal Biochem. 1999, 266(1):66-76.

[11] *O.I. Antimonova, N.A. Grudinina, V.V. Egorov, D.S. Polyakov, V.V. Iljin, M.M. Shavlovsky.* Interaction of the dye Congo red with fibrils of lysozyme, beta2- microglobulin and transthyretin, Tsitologiia, 2016, 58 156–163.

[12] *A.J. Howie, D.B. Brewer, D. Howell, A.P. Jones.* Physical basis of colors seen in Congo red-stained amyloid in polarized light. Laboratory investigation; a journal of technical methods and pathology, 2008, 88(3), 232–242.

[13] *B. Ranjbar, P. Gill.* Circular Dichroism Techniques: Biomolecular and Nanostructural Analyses- A Review. Chemical Biology & Drug Design, 2009, 74: 101-120.

[14] *E.I. Yakupova, L.G. Bobyleva, I.M. Vikhlyantsev, A.G. Bobylev.* Congo Red and amyloids: history and relationship, Biosci Rep. 2019, Jan 15;39(1)

Received: 20.07.2023

A NEW METHOD FOR SYNTHESIS OF CdTe NANOPARTICLES BY LASER RADIATION

M.A. JAFAROV[2], V.M. SALMANOV[2], A.G. GUSEINOV[1,2], G.B. IBRAGIMOV[1,2], R.M. MAMEDOV[2], T.A. MAMEDOVA[2], F.Sh. AKHMEDOVA[2]

[1]Institute of Physics, Ministry of Science and Education of the Republic of Azerbaijan
AZ 1143, G. Javid Avenue 131, Baku, Azerbaijan
[2]Baku State University, AZ1148 Baku, Azerbaijan
e-mail: vagif_salmanov@yahoo.com

The synthesis of CdTe nanoparticles using $CdCl_2$ and TeO_2 solutions under the action of laser radiation was experimentally studied. The radiation source was a pulsed Nd:YAG laser with built-in generators of the 2nd and 3rd harmonics, designed to generate radiation with a wavelength of 1064, 532, and 335 nm. The laser pulse duration was 10 ns with an energy of 135 mJ per pulse. In a colloidal solution, the formation of nanoparticles with a diameter of 10 to 50 nm was observed. X-ray diffraction analysis established that the crystal structure of the nanoparticles is the same as that of the bulk material (hexagonal). It is shown that the photoluminescence emission of the obtained nanoparticles has a green color (~510 nm) and is associated with the radiative recombination of free excitons.

Keywords: CdTe nanoparticles, laser ablation, photoluminescence.
PACS: 78.20.−e; 78.40.−q

1. INTRODUCTION

Among the most common semiconductor nanoparticles of groups II–VI, CdTe nanocrystals are of great interest for applications in optoelectronics, solar cells, LEDs, and biology [1–5]. Due to the developed surface (in a 1 nm particle, almost all atoms are surface atoms) and the manifestation of the quantum confinement effect [6], nanosized semiconductors have unique optical, electronic, catalytic, and other properties that are attractive to researchers. For example, solar cells based on nanosized cadmium telluride demonstrate a record efficiency of solar energy conversion and are currently considered more promising for mass application compared to traditional silicon batteries [7, 8]. To obtain nanoclusters and nanostructured materials, various methods are used - gas-dynamic, chemical, plasma, beam [9-18]. CdTe nanocrystals in solution are most often obtained by chemical synthesis using organometallic "precursors". These methods provide nearly monodisperse nanocrystals that exhibit narrow photoluminescence emission (up to ~30 nm) as well as high quantum yields. However, in general they require the use of expensive, pyrophoric, hazardous chemical precursors, as well as high temperatures and long reaction times.

One of the most promising methods for the synthesis of clusters is pulsed laser ablation (PLA) [1, 4]. Its main advantage is the ability to exclude the presence of foreign impurities in synthesized nanostructures, which is especially important for applications (one foreign atom in a 2 nm particle corresponds to a defect concentration of ~1021 cm–3 and can significantly change its properties). The advantages of the PLA method also include its flexibility and the ability to control the process of cluster growth. The formation of nanoclusters during PLA can occur according to two different scenarios: aggregation of the initial ablation products (atoms, molecules) in an expanding laser plasma and direct emission from the irradiated surface. Recently, significant progress has been made in the PLA synthesis of single-component semiconductor nanoclusters with controlled size, shape, and optical properties [19, 20], as well as in the understanding and quantitative description of the cluster formation process [21–23]. Laser ablation of nanoparticles in a liquid has attracted great interest due to its simplicity, the absence of the need for surfactants, and good control of the size and shape of synthesized nanoparticles [24-27]. In this method, many parameters, such as laser radiation flux density, laser radiation wavelength, pulse duration, and type of colloidal solution, can affect the characteristics of synthesized nanoparticles.

It should be noted that in all the above works devoted to laser ablation, bulk CdTe crystals grown by the Bridgman method were used as target materials. Laser ablation was carried out either in a vacuum or by immersing the target in various liquids, using ultrashort nano and femtosecond laser pulses. Indeed, the synthesis of CdTe nanoparticles by laser ablation, as noted, has great advantages over other methods. However, it should be taken into account that this method requires the growth of undoped CdTe crystals, which is by no means a simple technological problem. In this work, we propose a new method for obtaining nanoparticles, direct interaction of laser radiation with solutions that make up the components of CdTe nanoparticles. As shown by our experimental studies, the structural characteristics and optical properties of CdTe nanoparticles are significantly superior to those of nanoparticles obtained using a solid target.

2. EXPERIMENTAL METHODS

CdTe nanoparticles were synthesized in solution using the reactive laser ablation method. Highly pure $CdCl_2$ and TeO_2 powders mixed with distilled water

131, H.Javid ave, AZ-1143, Baku
Institute of Physics
E-mail: jophphysics@gmail.com

were used as initial raw materials. The reaction proceeded according to the following formula:

$$2CdCl_2+2TeO_2+2H_2O= 2CdTe+ 4HCl + 3O_2 \quad (1)$$

Immediately after irradiation with a laser pulse, CdTe nanoparticles were formed. The ablation process was performed by laser radiation with a wavelength of λ=1064 nm, with a pulse energy of 135 mJ and an ablation time of ~10 min. The radiation source was a pulsed Nd:YAG laser with built-in generators of the 2nd and 3rd harmonics, designed to generate radiation with a wavelength of 1064, 532, and 335 nm. The laser pulse duration was 10 ns with a maximum power of ~12 MW/cm^2. The radiation intensity was varied using calibrated neutral light filters. The optical absorption and luminescence spectra of CdTe nanoparticles were studied using an automatic M833 double dispersion monochromator (spectral resolution ~0.024 nm at a wavelength of 600 nm), with computer control and a detector that records radiation in the wavelength range of 350–2000 nm. The scheme of the experimental setup is shown in fig.1.

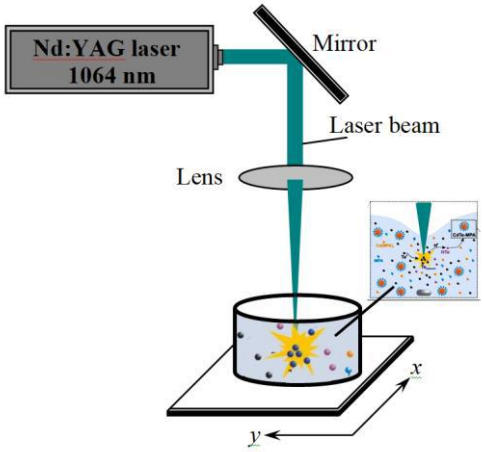

Fig. 1. Diagram of the experimental setup for ablation of GaSe nanoparticles.

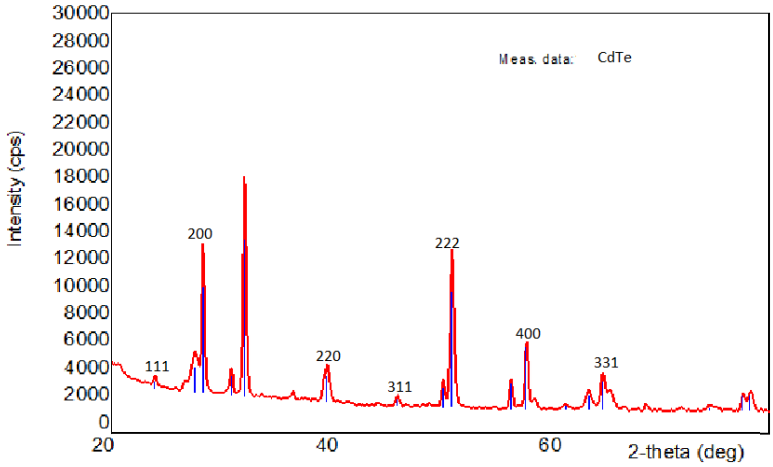

Fig. 2. Diffraction pattern (XRD) of CdTe nanoparticles on a glass substrate.

On figure 2 shows the diffraction pattern (XRD) of nanoparticles from drops of a CdTe colloidal solution dried on a clean glass substrate. CuK α, λ=1.544178A0 SSFOM: F17-610.0.5.10.60 were used as the radiation source.

It is shown that the diffraction planes (111), (200), (220), (311), (222), (400), (331), (422), and (511) at 2θ diffraction angles 23.62^0, 27.89^0, 38.97^0, 45.28^0, 49.34^0, 56.75^0, 63.60^0, 73.22^0, and 76.84^0, respectively, correspond to the cubic (zinc blende) structure of the bulk CdTe crystal [28], which confirms the crystal structure of the synthesized nanoparticles, which is the same as that of the bulk material.

Based on the X-ray diffraction patterns, using the Debye–Scherer formula [29], the sizes of the obtained nanoparticles were calculated:

$$D = \frac{k\lambda}{\beta \cos\theta} \quad (2)$$

where D – sizes of nanoparticles, k = 0.9 – line shape factor (shape factor), β = 0.035 A^0 – intensity maximum half-width (FWHM- Full Width at Half Maximum), λ – X-ray wavelength, λ=1.54 A^0, θ – Bragg angle, cosθ=0.727. Estimates show that the average size of CdTe crystallites is 27.434 nm (see Table 1).

Table 1.

Sizes of CdTe crystallites calculated using the Debye–Scherer formula

2 theta	Crystallite size
23.62(3) 111	28.27 nm
27.891(9) 200	34.91 nm
38.97(3) 220	16.31 nm
45.28(5) 311	23.66 nm
49.347(14) 222	39.72 nm
56.75(8) 400	47.17 nm
63.60(5) 331	20.78 nm
73.2(2) 422	10.87 nm
76.84(3) 511	25.22 nm
average crystallite size:	27.434 nm

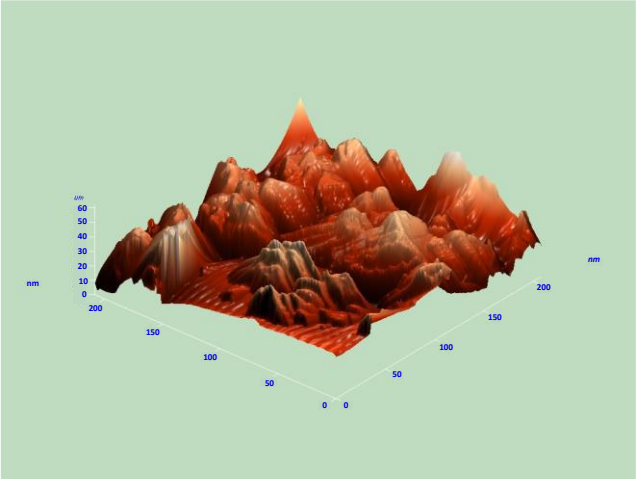

Fig. 3. AFM image of CdTe nanoparticles on a glass substrate.

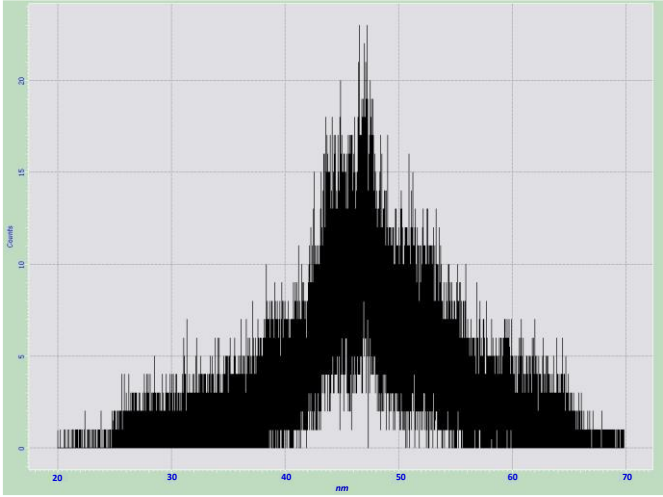

Fig.4. Histogram of particle size distribution.

The surface morphology of the synthesized CdTe nanoparticles was studied using AFM analysis. Figure 3 shows a 3D AFM image of CdTe nanoparticles on a glass substrate. As can be seen from the figure, a homogeneous distribution of particles in the presented figure is not observed.

The histogram of particle size distribution is shown in fig. 4. The average particle size estimated using the software was about 40-50 nm. The particle size value is higher than calculated by X-ray diffraction analysis. This is due to the fact that XRD depends on the free volume of dimensional defects, while AFM directly visualizes the grain without taking into account the degree of defectiveness of the crystal.

The absorption curve from a colloidal solution of

CdTe nanoparticles is shown in Figure 5a. The onset of absorption at ~500 nm is consistent with the absorption of an ensemble of nanoparticles whose maximum diameter is ~50 nm. Taking into account that CdTe is a semiconductor with a direct band gap, from dependence $\alpha^2 \sim f(h\nu)$, the band gap of the studied samples was determined, which turned out to be equal to E_g=2.46 eV (Fig. 5b). This value is 0.97 eV larger than the band gap of a bulk undoped CdTe crystal, (E_g=1.49 eV (~827 nm) [1]. It should be noted that the shift of the red absorption band of nanoparticles to the short-wavelength region of the spectrum compared to a bulk crystal is a characteristic feature semiconductor nanoparticles, which is associated with the quantum size effect.

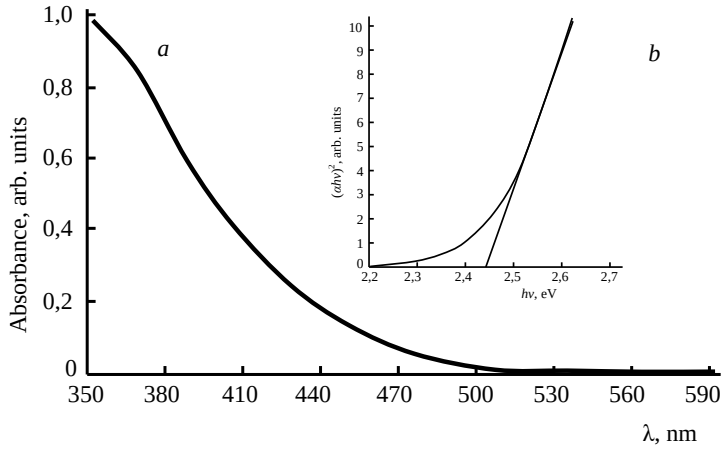

Fig. 5. Optical absorption spectrum (a) and $\alpha^2 \sim f(h\nu)$ dependence (b) of CdTe nanoparticles obtained in a colloidal solution.

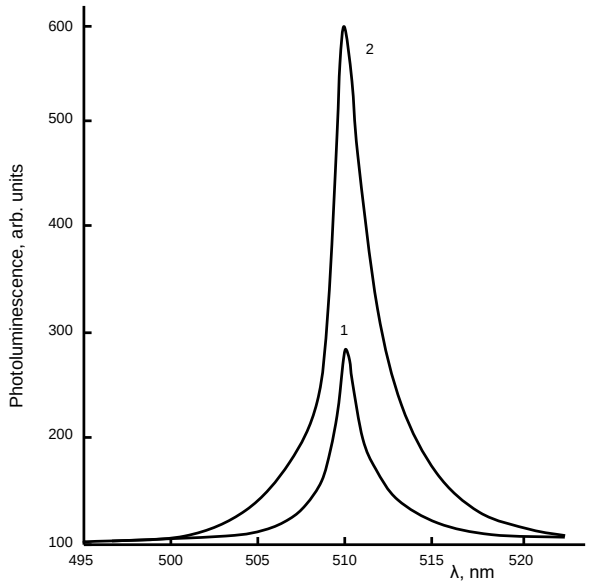

Fig.6. Photoluminescence spectra of CdTe nanoparticles at two different excitation powers, the second harmonic of a neodymium laser ($\hbar\omega = 2.34$ eV): 1 – 1 MW/cm^2; 2 – 10 MW/cm^2.

Figure 6 shows the photoluminescence spectra of CdTe nanoparticles excited by the second harmonic of the Nd:YAG laser ($\hbar\omega = 2.34$ eV). As can be seen from the figure, the emission maximum of nanoparticles corresponds to wavelengths ~ 510 nm (2.43 eV). An increase in the laser light power by 1.2 times does not affect the position of the spectra, but leads to an increase in the radiation intensity by ~2.1 times.

As regards the nature of the observed radiations, in our opinion they are due to the radiative recombination of free excitons. Knowing the energy of free excitons in CdTe (E_{ex} ~29 meV), it is possible to determine the band gap of nanoparticles $E_g = h\nu + E_{fr.ex.}$, which is equal to 2.46 eV, which is in satisfactory agreement with the value determined from the absorption spectrum.

3. CONCLUSION

A new method for synthesizing CdTe nanoparticles by laser radiation is proposed. Highly

pure $CdCl_2$ and TeO_2 powders mixed with distilled water were used as initial raw materials. The ablation process was performed by laser radiation with a wavelength of 1064 nm, with a pulse energy of 135 mJ and an ablation time of ~10 min. Under these ablation conditions in a colloidal solution, the formation of nanoparticles with diameters from ~10 to ~50 nm was observed. It is shown that the synthesized nanoparticles retain the crystalline structure of the bulk material and emit photoluminescence at 510 nm associated with the radiative recombination of free excitons.

[1] *N.G. Semaltianos, S. Logothetidis, W. Perrie, S. Romani, R.J. Potter, M. Sharp, G. Dearden and*

[2] *K.G. Watkins.* CdTe nanoparticles synthesized by laser ablation. Applied physics letters. 95, 2009, 033301-033306.

[3] *M. Gao, S. Kirstein, H. Möhwald, A.L. Rogach, A. Kornowski, A. Eychmüller, and H. Weller*. Strongly photoluminescent CdTe nanocrystals by proper surface modification. J. Phys. Chem. B 102, 1998, 8360.

[4] *L. Rogach.* Nanocrystalline CdTe and CdTe(S) particles: Wet chemical preparation, size-dependent optical properties and perspectives of optoelectronic applications. Mater. Sci. Eng., B 69, 2000, 435.

[5] *A.V. Bulqakov, A.B. Yevtushenko, Yu.Q. Shukhov, I. Ozerov, V. Marin.* «Quantum electronics», 40, № 11, 2010, 1021-1033.

[6] *Y. Luo, T. Tan, S. Wang, R. Pang, L. Jiang, D. Li, J. Feng, H. Zhang, S. Zhang, Ch. Li*. Ligand-Induced Nucleation Growth Kinetics of CdTe QDs: Implications for White-Light-Emitting Diodes. ACS Applied Nano Materials**.** *5* (1), 2022, 401.

[7] *H. Haug, S.W. Koch.* Quantum Theory of the Optical and Electronic Properties of Semiconductors. Singapore: World Scientific Publishing, 1994.

[8] *A. Morales-Acevado.* Thin film CdS/CdTe solar cells: research perspectives. Solar Energy, 80, 2006, 675.

[9] *K. Zweibel*. Engineering. The impact of tellurium supply on cadmium telluride photovoltaics. Science, 328, 2010, 699.

[10] *R.L. Johnston*. Atomic and Molecular Clusters. London: CRC Press, 2002. 256.

[11] *B.M. Smirnov.* Generation of cluster beams. Advances in the physical sciences, 173, 2003,609.

[12] *Q.N. Makarov.* Extremal processes in clusters in collision with a solid surface. Advances in the physical sciences, 176, 2006,121.

[13] *C.B. Murray, D.J. Norris, and M.G. Bawendi*. Synthesis and characterization of nearly monodisperse CdE (E = sulfur, selenium, tellurium) semiconductor nanocrystallites. J. Am. Chem. Soc. 115, 1993, 8706.

[14] *L. Rogach, L. Katsikas, A. Kornowski, D. Su, A. Eychmüller, and H. Weller, Ber. Bunsenges.* Synthesis, morphology and optical properties of thiol-stabilized CdTe nanoclusters in aqueous solution. Phys. Chem. 101, 1997, 1668**.**

[15] *Z.A. Peng and X. Peng.* Formation of High-Quality CdTe, CdSe, and CdS Nanocrystals Using CdO as Precursor. J. Am. Chem. Soc. 123, 2001, 183.

[16] *G. Dance, A. Choy, and M.L. Scudder.* Syntheses, properties, and molecular and crystal structures of (Me4N)4[E4M10(SPh)16] (E = sulfur or selenium; M = zinc or cadmium): molecular supertetrahedral fragments of the cubic metal chalcogenide lattice. J. Am. Chem. Soc. 106, 1984, 6285.

[17] *M. Marc-Oliver Piepenbrock, Tom Stirner, Mary O'Neill and Stephen M. Kelly*. Growth dynamics of CdTe nanoparticles in liquid and crystalline phases. J. Am. Chem. Soc. 129, 24, 2007, 7674.

[18] *Martin Sharp.* CdTe nanoparticles synthesized by laser ablation. Applied Physics Letters. 95, 2009, 033302.

[19] *A.R. Albert, A.Y. John.* Colloids and Surfaces A: Physicochemical and Engineering Aspects . 279, 1-3, 2006, 121.

[20] *L. Patrone, D. Nelson, V.I. Safarov, M. Sentis, W.J. Marine.* Photoluminescence of silicon nanoclusters with reduced size dispersion produced by laser ablation. Appl. Phys., 87, 2000, 3829.

[21] *T. Seto, T. Orii, M. Hirasawa, N. Aya.* Fabrication of silicon nanostructured films by deposition of size-selected nanoparticles generated by pulsed laser ablation. Thin Solid Films, 437, 2003, 230.

[22] *B. Lukyanchuk, W. Marine.* On the delay time in photoluminescence of Si-nanoclusters, produced by laser ablation. Appl. Surf. Sci., 314, 2000, 154.

[23] *S.I. Anisimov, B.S. Lukyanchuk*. Selected problems of the theory of laser ablation. Advances in the physical sciences, 172, 2002, 301.

[24] *A.V. Bulgakov, I. Ozerov, W. Marine*. Silicon clusters produced by femtosecond laser ablation: non-thermal emission and gas-phase condensation. Appl. Phys. A, 79, 2004, 1591.

[25] *S. Xu, J. Ziegler, T.J. Nann.* Rapid synthesis of highly luminescent InP and InP/ZnS nanocrystals. Mater. Chem., 18, 2008, 2653.

[26] *I. Ozerov, D. Nelson, A.V. Bulgakov, W. Marine, M. Sentis.* Synthesis and laser processing of ZnO nanocrystalline thin films. Appl. Surf. Sci., 349, 2003, 212.

[27] *S. Neretina, P. Mascher, R.A. Hughes, N. Braidy, W.H. Gong, J.F. Britten, J.S. Preston, N.V. Sochinskii, P. Dippo.* Evolution of wurtzite CdTe through the formation of cluster assembled films. Appl. Phys. Lett., 89, 2006, 133101.

[28] *J. Bonse, M. Munz, H.J. Sturm.* Structure formation on the surface of indium phosphide irradiated by femtosecond laser pulses. Appl. Phys., 97, 2005, 013538.

[29] JCPDS, International Centre for Diffraction Data, USA, Card Number 15-0770.S. Samuel. Nanolasers: lasing from nanoscale quantum wires Int. J. of Nanotechnology 1, 2004, 42-85.

Received: 10.07.2023

MAIN ELEMENTS AND CHARACTERISTICS OF ELECTROHYDRODYNAMIC ION SOURCES BASED ON InSb

S.A. ALIYEV, F.E. MAMMADOV, E.M. AKBEROV, I.I. GURBANOV, A.A. BADALOV, Sh.O. EMINOV

Institute of Physics, Ministry of Science and Education of the Republic of Azerbaijan
AZ 1143, G. Javid Avenue 131, Baku, Azerbaijan
sabir.eliyev.1950@mail.ru

For the first time, the method of preparation of the main constructive elements of the ion source used for obtaining ion beams with high current density based on InSb and $InSb_{0.98}Bi_{0.02}$ was developed and the volt-ampere characteristic of its ion current was measured. The material of the needle, which is the main element of the source, was selected according to the working substance (InSb and $InSb_{0.98}Bi_{0.02}$), the needle was sharpened by mechanical and chemical methods, and then wetted in the melt of the working substance at $550°C$ in a vacuum. The sharpened and wetted needles are placed in a closed graphite container, which is another element of the ion source, with the working substance inside. During the process, we ensured that the tip of the needle extended into the ion emission zone. Batches of InSb and $InSb_{0.98}Bi_{0.02}$ ions with different mass and charge were obtained in the prepared ion source.

Keywords: electrohydrodynamic sharp ion source, working substance, liquid metal ion source.
PACS: 29.25.Ni; 52.25.Tx; 81.16.Rf

INTRODUCTION

Electrohydrodynamic (EGD) or liquid metal ion sources based on alloys (LMAIS) allow for the generation of atomic and molecular (cluster) ion currents of various elements and their chemical compounds with densities of up to hundreds of millions $\sim 10^8 A/sm^2$and low energy spread. The main characteristics of EGD sources and their differences from a wide range of gas, plasma, and other types of ion sources are analyzed in detail in [1,2]. In the field of micro and nanotechnology, electrohydrodynamic ion sources are indispensable for sub-micrometer lithography, ion-stimulated chemical synthesis, implantation, and microanalysis [3]. Today, it is impossible to conceive of the formation, analysis, and processing of a desired surface relief with sub-micrometer resolution without a focused ion beam [4,5]. Initially, pure metals with low melting temperatures, such as gallium, indium, etc., were used as the working substances for EGD emitters [6]. However, the solution to many modern technological challenges, such as localized ion implantation, ion beam mixing, direct non-resistive ion lithography, and the fabrication of micro and nanoelectromechanical systems, is impossible without the utilization of ion beams with varying masses, charge states, and chemical properties [7]. This has stimulated the development of liquid metal ion sources based on alloys, enabling the generation of a broad spectrum of different ions [8]. The utilization of eutectic alloys with different compositions has allowed for a more predictable and controllable alteration of the electrical, optical, magnetic, and mechanical properties of the processed materials. LMAIS and subsequently LMAIS based on alloys are also extensively employed in secondary ion mass spectrometry and secondary neutral particle analysis [9], as well as in space technology and ion microscopy [10].

In recent times, surface processing with ion beams is almost exclusively conducted using electrohydrodynamic ion sources. The fact that the emission zone of liquid metal ion sources is very small creates favorable opportunities for the application of these sources in technologies aimed at producing various surface structures and thin films. Considering that the types of ions used significantly influence the physicochemical properties of the obtained microscale structures, including electrical, optical, magnetic, and mechanical properties, it can be asserted that a large potential application area has emerged, which can be regulated through appropriate selection. As a result of research conducted in this field over the past half-century, almost half of the chemical elements from the periodic table have been found to be potentially suitable or already utilized in modern LMAIS [2, 4].

The presented article elucidates the peculiarities of manufacturing elements for electrohydrodynamic ion sources using InSb as the working substance. It provides the results of scientific research on certain specific characteristics of ion beams generated from these sources.

EXPERIMENT

One of the main components of liquid metal ion sources is a sharp-tipped needle. The needle is wetted with the working substance, and upon subsequent heating, the working substance melts and flows along the surface of the needle towards its pointed end. Depending on the working substance, the material of the needle should be chosen to be refractory, wettable by the working substance, resistant to dissolution in it, and chemically inert towards it. It should also maintain the shape of its tip for a sufficient duration without undergoing erosion. Moreover, the melting temperature of the needle material should be higher than that of the working substance. The voltage at which ion emission occurs and the longevity of the needle directly depend on its sharpness. Needles can be fabricated through both mechanical and electrochemical means. However, since mechanically sharpened needles require a relatively high threshold voltage for ion emission, electrochemical sharpening is preferable.

131, H.Javid ave, AZ-1143, Baku
Institute of Physics
E-mail: jophphysics@gmail.com

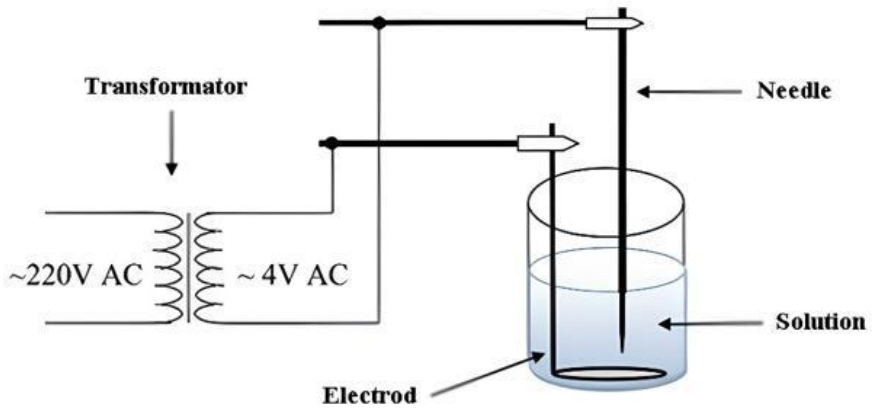

Fig. 1. Process of chemical preparation of the needle.

Figure 1 illustrates the process of chemical preparation of the needle. Prior to the procedure, the choice of chemical solution is determined based on the needle material. In our experiments, we used nickel-chromium (NiCr) needles and selected a 6% solution of HCl. The solution is poured into a specialized container containing an electrode. A constant voltage of approximately 4V is applied between the needle and the electrode. Subsequently, the needle is quickly immersed in the solution for several minutes and then removed. The tip of the needle is observed through a magnifying glass during the procedure. When using a constant voltage in the experiments, the sharp end of the needle becomes smooth, creating favorable conditions for the melted liquid to flow towards the tip of the needle.

In our experiments, tungsten or nichrome needles with a diameter of (0.5-0.8) mm were sharpened by mechanical or electrochemical means to a tip radius of several (30-50) μm. Diamond files and the finest sandpaper were used for mechanical wire processing. To ensure continuous delivery of the working substance to the needle tip and its further emission, the needle needs to be sharpened along its axis with the creation of longitudinal grooves. This facilitates the flow of the working substance along the grooves. The needle can also be sharpened by electrochemical means. In this case, for each needle material, the electrochemical treatment requires the selection of an appropriate electrolyte composition.

To wet the NiCr needle with the working substance, it is placed in a narrow graphite boat, and InSb is poured onto the sharp end. The boat is covered with a graphite lid and heated under vacuum conditions until the InSb melts and wets the needle with the working substance (see Figure 2). The experiment was conducted using a Leybold-Heraeus L-700-Q vacuum setup.

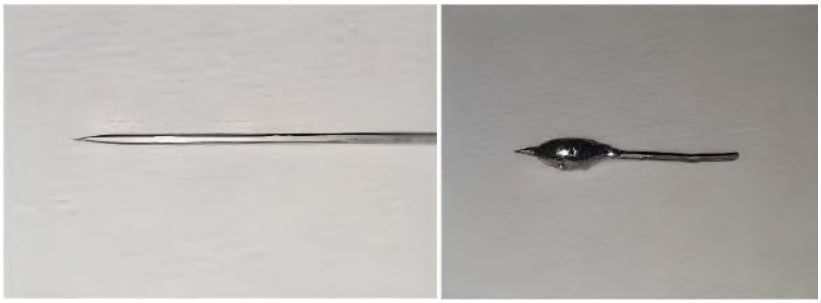

a) b))

Fig. 2. a) A NiCr needle sharpened in a chemical solution. b) A NiCr needle saturated with the working substance InSb.

For conducting research with a liquid metal ion source, a special container-type structure was designed and manufactured. This structure allowed the generation of ion beams of In, Sn, Au, Ge, B, as well as alloys such as InSb and $InSb_{0.98}Bi_{0.02}$. Inside the container, a needle made of a refractory material was placed, wetted with the working substance. The tip of the needle protruded from a small opening in the container, leading to the emission zone (see Figure 3). The material of the needle was selected for each working substance to ensure reliable wetting of its surface.

To achieve ion emission, the wetted needle is placed in a specially designed container. Containers are made from various materials with high melting points, such as titanium, molybdenum, graphite, etc. In our case, we used graphite as the container material. The choice of graphite as the container material is based on several properties of graphite. Graphite exhibits negative thermal expansion along its basal plane up to a temperature of 700 K. As a result, when the volume of the container housing the needle decreases, the electrical contact between the needle and the positive pole of the applied accelerating field is further enhanced.

Fig. 3. A needle made of nickel-chromium wire, impregnated with InSb, is placed inside a graphite container.

This leads to the formation of a high-intensity electric field between the needle and the extractor. At high temperatures, graphite does not melt due to its physical properties and naturally does not mix with the working substance. Additionally, the technical processing of graphite does not pose significant difficulties compared to other refractory materials. As a result, the obtained ion beam is homogeneous, consisting solely of particles of the working substance.

In such a design, the working substance is contained in a closed volume, minimizing the evaporation of the melt, which occurs only from the surface of the needle tip and the opening in the container. The consumption of the working substance in the form of ions is very small, so its mass supply can be less than one gram, and accordingly, the container size needs to be small. This is also necessary in terms of power consumption required to heat the container to a high temperature for melting the working substance. To achieve a high temperature of the container (around 1000°C), it is necessary to limit the heat dissipation of the supplied energy. Therefore, a structure was created to secure the container using three thin tantalum spokes. Each spoke has a cross-sectional area of only 1 mm², but the system proved to be sufficiently rigid and resistant to thermal loads. Calculation based on the heat conduction equation was performed to ensure efficient heat transfer and maintain the desired temperature.

$$Q = \lambda \frac{\Delta T}{l} S$$

(where λ is the average thermal conductivity of tantalum, S is the cross-sectional area, l is the length of the heat sink) shows that in order to heat the container to the desired temperature in this design, an electron bombardment power of about 30 W is required. The container has a diameter of 6 mm and a height of 10 mm. It is made of graphite, which is non-wetting to most liquids and has a low vapor pressure.

Local heating of the graphite container with the needle and the working substance is achieved by electron bombardment from the rear side using a tungsten filament heated to the melting temperature of the working substance. With a diameter of 0.5 mm for the tungsten filament, a filament current of approximately 20 amperes was necessary to heat it to the thermo-electron emission temperature. The container holder is attached to a copper anode cylinder, and both the anode cylinder and the cathode holders are cooled by flowing water.

A schematic representation of the liquid metal ion source is provided in Figure 4. A needle made of NiCr material with a tip radius of a few micrometers is placed inside a graphite container and heated to the melting temperature of the working material. The extractor is located at a distance of 1 mm from the needle. With a potential difference between the needle and the extractor of 5-6 kV, ion emission occurs, and a bright spot is observed near the sharp end of the needle. The ion beam is dispersed at an angle of approximately 90 degrees, and the beam current is registered in the collector circuit.

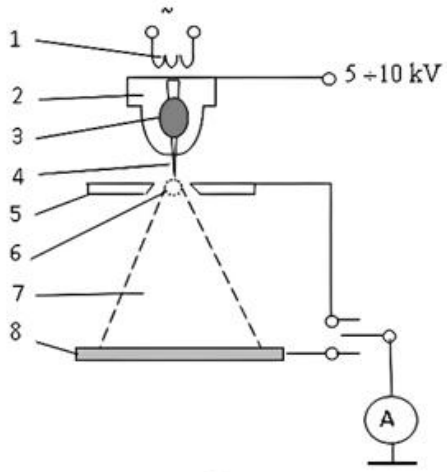

Fig. 4. Ion Source Diagram
1 - Cathode, 2 - Container, 3 - Working substance, 4 - Needle, 5 - Extractor, 6 - Bright area, 7 - Ion beam, 8 – Collector

The use of graphite as the material for the container is justified by its properties. Graphite has a negative thermal expansion in the direction of its basal plane up to a temperature of 700 K. As a result, when the volume of the container housing the needle decreases, the electrical contact between the needle and the positive pole of the applied accelerating field is improved. This leads to the formation of a high-

intensity electric field between the needle and the extractor. At high temperatures, graphite does not melt and naturally does not mix with the working substance due to its physical properties. Furthermore, the technical processing of graphite does not pose significant challenges compared to other refractory materials. Therefore, the resulting ion beam is homogeneous and consists only of particles of the working substance. One of the key indicators of the performance of any liquid metal ion source (LMIS) is its volt-ampere characteristic (VAC), which provides the functional relationship between the emission current of ions (I) and the extracting voltage (U) applied to the extractor. Proper interpretation of the VAC allows us to accurately assess the suitability and reliability of the LMIS in all operating modes, both after the source's manufacturing and after its long-term use. This issue has always been given special attention in experimental and theoretical studies [4,11]. According to the widely accepted theoretical model by Mayer, the ion emission current for a threshold potential difference is determined by the formula

$$I = 3\pi\sqrt{\frac{2e}{m}}\frac{r\gamma\cos\alpha}{\sqrt{U_{min}}}\left(\frac{U}{U_{min}} - 1\right)$$

From the formula, it can be seen that the ion emission current is influenced by the potential difference U at the extractor, the atomic mass of the generated ions m, the surface tension of the working fluid γ, the radius of curvature of the emitter r, and the Taylor cone angle α. Ion emission begins when the threshold voltage is exceeded. The nature and slope of the VA characteristics of the needle-shaped LMIS depend on the distance between the source and the extractor, the aperture diameter in the extractor, and the emitter material. The influence of electrode geometry on the volt-ampere characteristics of LMIS has been extensively studied in [12]. On Figure 5, the volt-ampere characteristics are shown for the alloys InSb and $InSb_{0,98}Bi_{0,02}$.

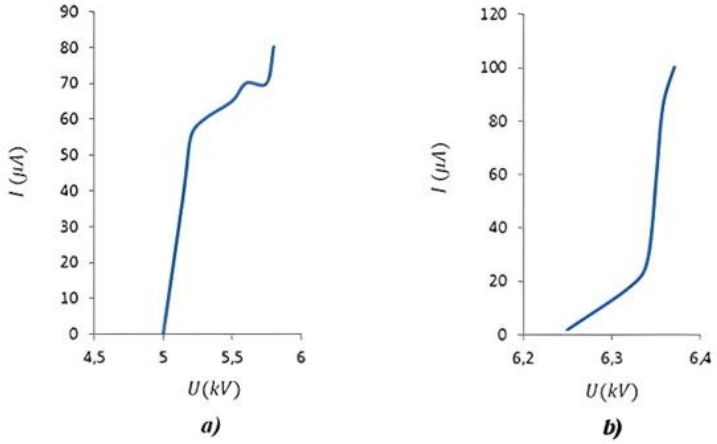

Fig. 5. a) Volt-ampere characteristic (VAC) of the ion source with the working substance InSb; b) VAC of the ion source with the working substance $InSb_{0,98}Bi_{0,02}$.

We used smooth needles, which results in a steeper slope of the VAC. Additional factors include the angle and radius of the needle tip, as well as the diameter of the needle base. As seen in the figure, for both samples, ion emission begins at a threshold voltage and increases with increasing extraction voltage. For the InSb0.98Bi0.02 alloy, the threshold voltage is higher than that of InSb, which is likely due to the higher melting temperature of Bi.

To form the Taylor cone, a higher voltage is required compared to maintaining it. Therefore, the optimal operating emission current is considered to be the one at which the extraction voltage is higher. At this voltage, the emission current is higher with larger tip radius, needle base diameter, and taper angle. The shape of the VAC is significantly influenced by the physicochemical properties of the alloys, such as density, surface tension, surface free energy, sublimation heat, and operating temperature.

CONCLUSION

For the first time, a liquid metal ion source based on these materials was developed to obtain ion beams of InSb and $InSb_{0.98}Bi_{0.02}$ with different masses, charge states, and chemical properties. In accordance with the physicochemical properties of these working substances, a nichrome wire (NiCr) with a diameter of 0.5 mm was used as the material for the needle. The needles were sharpened using electrochemical and mechanical methods to achieve a tip size of (50-70) μm, and they were wetted with the working substance under vacuum conditions at a pressure of $P = 2 \times 10^{-5} mbar$.

The prepared needles, along with additional working material, were placed in a sealed graphite container, which also serves as another primary element of the ion source. The entire experimental system was assembled on the basis of the A-700-Q Leybold-Heraeus vacuum setup. For each working substance, InSb and $InSb_{0.98}Bi_{0.02}$, functional dependencies of the current emission (I) on the extraction voltage (U) were obtained for the first time.

[1] *V.T. Cherepin.* Ion microprobe analysis. Kiev, Naukova Dumka, 1992.
[2] *V.G. Dudnikov.* Rev. Sci. Instrum. 67 915, 1996.
[3] *A.I. Zhakin.* Phys. Usp. 56 141, 2013.
[4] *L. Bischoff et. al.* Appl. Phys. Rev. 3 021101, 2016.
[5] *J. Gierak at. el.* J. Vac. Sci. Technol. B. 36 06J101, 2018.
[6] *N. Bassim, K. Scott, L.A. Giannuzzi.* MRS Bull. 39 317, 2014.
[7] *L. Bruchhaus et.al.* Appl. Phys. Rev. 4 011302, 2017.
[8] *P. Mazarov, V.G. Dudnikov, A.B Tolstoguzov.* "Electrohydrodynamic emitters of ion beams" *Phys. Usp.* 63, 1219–1255, 2020
[9] *Tajmar et al.* Ultramicroscopi 109 442, 2009.
[10] *G. Hlawacek, A. Göltzhauser.* (Eds) Helium ion Mikroskopi (Cham: Springer İntern. Publ., 2 016)
[11] *R.G. Forbes, Mair G.L.R.,* in Handbook of Charged Particle Optics (Ed. J. Orloff) 2nd ed. (Boca Raton, FL: CRC Press, Taylor and Francis, 2009, p. 29.
[12] *Bell A.E., Swanson L.W.* Appl. Phys. A 41 335, 1986.

Received: 07.07.2023

Si - Bi_2Te_3 PHOTOCONVERTER DETECTORS

G.M. AHMADOV[a], G.B. IBRAGIMOV[a,b], M.A. JAFAROV[b]
[a]Institute of Physics, Ministry of Science and Education of the Republic of Azerbaijan
AZ 1143, G. Javid Avenue 131, Baku, Azerbaijan
[b]Baku State University, Baku, Azerbaijan, Maarif.Jafarov@mail.ru

Bismuth telluride (Bi_2Te_3) photoconverter detector based on Si single crystal is presented. The photo-reactions of the obtained photodetectors in infrared radiation with wavelengths of 1064 nm and 1550 nm were studied at room temperature. Linear dependences of the photocurrent on both the power of the incident light and the applied voltage were observed. Key device parameters, including photosensitivity and quantum efficiency, were calculated.

Keywords: Bismuth telluride, Thin films, electrochemical deposition, photoconductive detector.
PACS: 71.55Gs, 78.20.-e.

INTRODUCTION

The integrated circuit (IC) industry has rapidly developed following Moore's Law for over half a century. However, Moore's law is reaching its end when the transistors are finally scaled down to several nanometers, and the quantum effects and heat dissipation problems have become dominant [1-3]. Silicon (Si) photonics have emerged as one of a few potential technologies to extend the lifetime of Moore's Law, or, in other words, to open the "post Moore era" [4,5]. Si photonics can provide high transmission speed, high bandwidth, low power consumption, low heat dissipation, etc., utilizing the advantages of light over electrons. In recent years, many significant breakthroughs of Si based passive and active building blocks on and in Si have been demonstrated including waveguides, electro-optic modulators, ultrafast photodetectors, fiber-to-waveguide couplers, and lasers [7]. Among all the elementary components, a high performance near infrared photodetector is crucial to make a high speed optical link for either optical telecommunications or interconnects [8]. Conventionally, there are two kinds of absorbent materials at the telecom wavelength utilized for photon detection on Si: germanium (Ge)-on-Si[5] and III-V-on-Si [9]. Here, we have put forward a topological insulator (TI) based photodetector on Si, which is compatible with complementary metal-oxide-semiconductor (CMOS) technology and can be monolithically integrated on Si.

Bismuth telluride (Bi_2Te_3) together with Bi_2Se_3 and Sb_2Te_3 was theoretically predicted and experimentally proved to be a typical 3-dimensional (3D) TI with a single Dirac cone on the surface. Molecular beam epitaxy (MBE), chemical vapor deposition [10], and pulsed laser deposition techniques [11] have been adopted in the fabrication of high-quality TI films of Bi_2Se_3, Bi_2Te_3, and Sb_2Te_3 on substrates including sapphire [12], $SrTiO_3$[13], and also Si.

Many theoretical studies have been focused on the response of the surface states to light, and several worthy progressive studies have been reported, including the Dirac surface state assisted high-performance broadband photodetection from infrared to terahertz [14], the circularly polarized light induced helicity-dependent current [15], the nonlinearity induced passive mode-locked lasers [16], the warping effect enhanced relative signal-to-noise ratio (SNR) [17], and the linearly polarized light induced polarization dependent photocurrents[18].

Zhang et al [19]. predicted that the surface state can have strong optical absorption. The surface absorption is determined by the fine-structure constant *a*, and it is uniform and independent of the wavelength.

In this letter, Si-based Bi_2Te_3 photodetectors with responses to 1064 nm and 1550 nm light illumination at room temperature are demonstrated. This study shows that TI based photodetectors could be one of the candidate detectors for future Si photonics.

EXPERIMENT

The following conditions were used to prepare the electrolyte solution used. According to the Pourbaix diagrams, in pH=0 solutions, Bi and Te exist as completely dissolved Bi^{3+} and $HTeO_2^+$, respectively. The electrolyte was prepared with water (18 MΩcm resistivity) collected from Barnstead E-pure filtration system. First $Bi(NO_3)_3.5H_2O$ (purity 99% analytical grade, Aldrich-Sigma) and TeO_2 (purity 99%) were dissolved in 1M HNO_3. The two solutions were then mixed and the mixture was adjusted to pH=6. All electrochemical depositions were done at room temperature using conventional three–electrode system and a potentiostat (Gamry Reference 600). PTFE reaction cell was used where the working electrode was placed horizontally at the bottom. Gold coated silicon wafer and Platinum mesh were used as working and counter electrodes, respectively. Ag/AgCl with 3M KCl electrolyte was used as the reference electrode. Bi_2Te_3 thin films were prepared by the continuous electrodeposition method of which a constant voltage was applied. The gold working electrode was made as a gold-coated silicon wafer (n-Si (111) with a resistivity < 0.02 Ω cm). This coating of gold on the silicon wafer was done by first cleaning the silicon wafer by ultra sonication in organic solvents. Then it was exposed to

131, H.Javid ave, AZ-1143, Baku
Institute of Physics
E-mail: jophphysics@gmail.com

a mild oxygen plasma treatment (PE/RIH, 50 W) for 2 min to remove the organic contamination and surface particles. Before this wafer was placed in the reaction cell, an In-Ga eutectic was coated on the unpolished backside of the silicon wafer as an ohmic contact.

Then, the Ti electrodes were achieved by electron beam evaporation on top of the Bi_2Te_3 film, which exhibits a linear dependence, suggesting that ideal Ohmic contacts were formed between the electrodes and the Bi_2Te_3 film from the I–V test in the dark.

RESULT AND DISCUTION

The incident power range for 1064 nm and 1550 nm was 0.67–2.8 mW and 0.194–0.389 mW, respectively. All the measurements were carried out at room temperature. The responsivity (R) and quantum efficiency (η) of this device were calculated according to the following equations, respectively [20]:

$$R = \frac{I_{ph}}{P_{opt}} \quad (1)$$

$$\eta = R\left(\frac{hc}{q\lambda}\right) \quad (2)$$

where I_{ph}, P_{opt}, h, c, q and k are the photocurrent, the light power of the effective illuminated area, the Planck's constant, the light velocity in vacuum, the electron charge, and the wavelength of incident light, respectively.

Figure 1 presents the AFM image of the Bi_2Te_3 film. The root mean square (RMS) roughness of the Bi_2Te_3 film is 1.29 nm. Surface steps with a height of 1 nm can be observed clearly, which correspond to the thickness of a quintuple layer with five Te-Bi-Te-Bi-Te atomic layers. The existence of clear surface steps indicates high crystal quality.

Photocurrent under different bias voltages and light powers was investigated, and the results after the removal of the background current are shown in Figure 2. Figures 2(a) and 2(c) present the photocurrent of a typical device under different incident powers at the wavelength of 1064 nm and 1550 nm, respectively. Obviously, the photocurrent exhibits a high dependence on the bias voltage and the incident light power. Along with the increasing bias voltage, an approximately linear increasing tendency of photocurrent can be observed. Given the fact that the bias voltage facilitates the separation and transport of photon-excited carriers, collection of photo- generated carriers will increase significantly with the increase in the electric field.

It is obvious that at the higher excitation intensity, more electron-hole pairs are generated, which is consistent with the observed fact that the photocurrent increases monotonously with the increase in the excitation power. In order to have a more intuitive observation of the photocurrent-excitation power relation, the photocurrent under different excitation powers at 0.1 V is plotted and linearly fitted in Figures 3(b) and 3(d) for 1064 nm and 1550 nm, respectively.

Based on Eq. (1), Eq. (2), and the slope of the linear fitting curve, the responsivity for the device is 3.64 x 10^{-3} AW^{-1} for 1064 nm and 3.32 x 10^{-2} AW^{-1} for 1550 nm, respectively. The quantum efficiency is 0.424% for 1064 nm and 2.66% for 1550 nm.

The relationship of the incident light intensity-absorption coefficient for Bi_2Te_3 follows Eq. (3), where I, I_O, a, and d represent the light intensity, original incident light intensity, absorption coefficient, and thickness of the Bi_2Te_3 film, respectively. There are two interfaces of the device, Bi_2Te_3 and Si and Bi_2Te_3 and air. Reflections exist for both the interfaces. The interfacial reflection coefficients between air and Bi_2Te_3 are up to 53% for 1064 nm and 60% for 1550 nm, while those between Bi_2Te_3 and Si are 7.8% for 1064 nm and 14.7% for 1550 nm.[24] The absorption coefficients for different incident light wavelengths are also distinct, which are 7.0 x 10^5 cm^{-1} for 1064 nm and 4.2 x 10^5 cm^{-1} for 1550 nm, respectively.

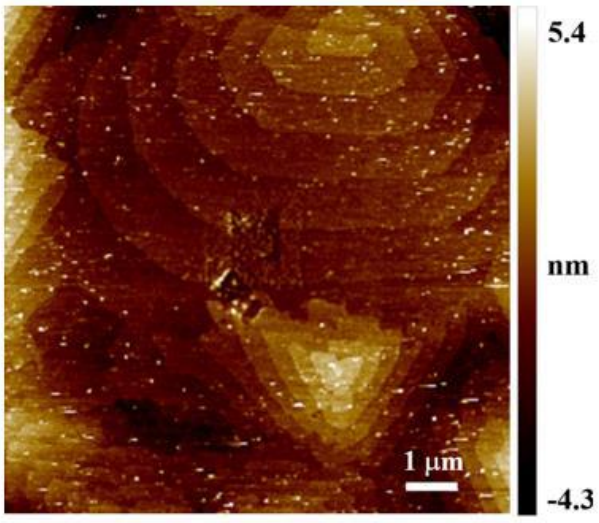

Fig. 1. AFM image of the Bi_2Te_3 film on Si.

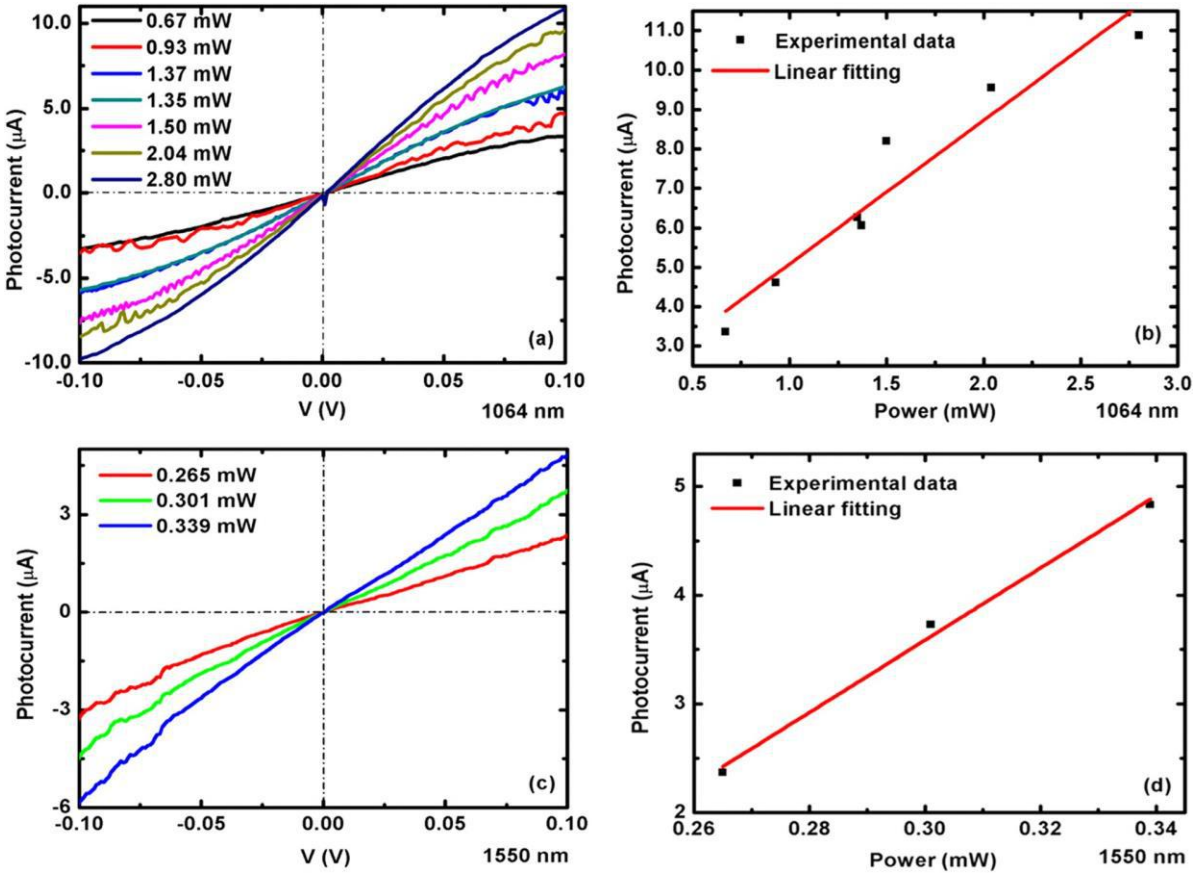

Fig. 2. Typical photocurrent-voltage curves of the Bi_2Te_3 photodetector at different incident powers under 1064 nm (a) and 1550 nm (c) illumination, respectively. (b) and (d) show the photocurrent under different excitation powers at 0.1 V corresponding to (a) and (c), respectively. The red line is a linear fit of the data points.

After multiple reflections, the relationship of the light intensity after absorption by the Bi_2Te_3 film and the original incident light intensity can be expressed by Eq. (4), where I_1, R_C, and R_C' represent the light intensity after absorption by the Bi_2Te_3 film, reflection coefficient between air and the Bi_2Te_3 film, and reflection coefficient between the Bi_2Te_3 film and Si, respectively.

$$I = I_O e^{-ad} \tag{3}$$

$$I_\infty = \frac{R_C + (1-R_C)(1-R'_C)e^{-ad}}{1-(1-R_C)R'_C e^{-2ad}} I_O \tag{4}$$

Obviously, the reflection of most of the incident light has been caused by the large reflection rate. Considering this non-negligible loss, the quantum efficiency can be revised by dividing 0.457 for 1064 nm and 0.358 for 1550 nm (the other portion is reflected by the interfaces and transmitted into Si). After revision, the internal quantum efficiency of the device is 0.9% under the wavelength of 1064 nm, and it corresponds to 7.4% for the case of 1550 nm. Under the same incident power, the longer wavelength leads to a larger number of photons, thereby a higher photocurrent and larger responsivity are expected. The performance of the present device in terms of responsivity and quantum efficiency is much better than those of the published polycrystalline Bi_2Te_3 based devices. The responsivity is 2–3 orders higher.

For Bi_2Te_3, the bandgap measured by angle-resolved photoemission spectroscopy is 0.165 eV while that for Si is 1.12 eV. The photocurrent would mainly consist of four parts: the photoconductivity effect of the Bi_2Te_3 bulk and the surface states, transitions between the surface states and the bulk states, and the contribution of Si. For illumination at 1064 nm, Si shows little absorption to the incident light since most light is absorbed by Bi_2Te_3 before reaching Si.

CONCLUSION

In summary, we reported a monocrystalline Bi_2Te_3 photoconductive detector on Si grown by electrochemical technology and can be monolithically integrated on Si. The as-fabricated photodetector exhibits a high response to photons at 1064 nm and 1550 nm at room temperature. The responsivity and the quantum efficiency are much better than polycrystalline Bi_2Te_3 based devices. The responsivity and the internal quantum efficiency of the device are 3.64×10^{-3} AW^{-1} and 0.9% for 1064 nm and 3.32×10^{-2} AW^{-1} and 7.4% for 1550 nm, respectively. This study suggests that the Bi_2Te_3 photodetectors have potential applications in future Si photonics.

[1] *M.M. Waldrop.* Nat.News 530, 144, 2016.
[2] *D. Liang and J.E. Bowers.* Nat.Photonics4, 511, 2010.
[3] *R. Soref.* IEEEJ. Sel. Top. Quantum Electron. 12, 1678, 2006.
[4] *Bothpho Osmond, D. Marris-Morini, P. Crozat, E. Cassan, J. M.F'ed'eli, S. Brision, J. F. Damlencourt, V. Mazzochi, D. Van Thourhout and J. Brouckaert.* in IEEE International Conference on Group IVPhotonics GFP. 2009, Vol. 1, p. 10.
[5] *L. Chen, P. Dong and M. Lipson.* V Opt. Express 16,11513, 2008.
[6] *S. Feng, Y. Geng, K. M. Lau, and A. W. Poon.* IEEE InternationalConference on Group IV Photonics GFP 2012, Vol. 37, p. 51.
[7] *Y.L. Chen, J.G. Analytis, J.H. Chu, Z.K. Liu, S.K. Mo, X.L. Qi, H.J. Zhang, D.H. Lu, X. Dai, Z. Fang, S. C. Zhang, I.R. Fisher, Z. Hussain, and Z.X. Shen.* Science 325, 178, 2009.
[8] *H. Zhang, C. Liu, X. Qi, X. Dai, Z. Fang, and S. Zhang*. Nat. Phys. 5,438, 2009.
[9] *Y.Y. Li, G. Wang, X.G. Zhu, M.H. Liu, C. Ye, X. Chen, Y.Y. Wang, K. He, L.L. Wang, X.C. Ma, H.J. Zhang, X. Dai, Z. Fang, X.C. Xie, Y. Liu, X.L. Qi, J.F. Jia, S.C. Zhang, and Q.K. Xue*. Adv. Mater. 22, 4002, 2010.
[10] *H. Cao, R. Venkatasubramanian, C. Liu, J. Pierce, H. Yang, M.Z. Hasan, Y. Wu, and Y.P. Chen.* Appl. Phys. Lett. 101,162104, 2012.
[11] *H. Zhang, J. Yao, J. Shao, H. Lu, S. Li, D. Bao, C. Wang, and G. Yang*. Sci. Rep. 4, 5876 (2014).
[12] *K. Zheng, L.B. Luo, T.F. Zhang, Y.H. Liu, Y.Q. Yu, R. Lu, H.L. Qiu, Z.J. Li, and J.C. Andrew Huang*, J.Mater. Chem. C3, 9154, 2015.
[13] *P.H. Le, K.H. Wu, C.W. Luo, and J. Leu.* Thin Solid Films 534,659, 2013.
[14] *X. Zhang, J. Wang, and S.C. Zhang*. Phys. Rev. B 82, 245107, 2010.
[15] *P. Hosur*. Phys. Rev.B83,035309 (2011).
[16] *J. Koo, J. Lee, C. Chi, and J.H. Lee.* J.Opt.Soc.Am.B31, 2157 (2014).
[17] *J. M. Shao, H. Li, and G.W. Yang.* Nanoscale6,3513, 2014.
[18] *J.D. Yao, J.M. Shao, S.W. Li, D.H. Bao, and G.W. Yang.* Sci.Rep.5,14184, 2015.
[19] *F. Xia,T. Mueller,Y. Lin, A. Valdes-Garcia, and P. Avouris.* Nat.Nanotechnol. 4, 839, 2009.
[20] *X. Gan, R. J. Shiue, Y. Gao, I. Meric, T. F. Heinz, K. Shepard, J. Hone, S.Assefa, and D. Englund*. Nat. Photonics 7, 883, 2013.

Received: 25.07.2023

EFFECTS OF THE HfO_2 NANOFILLER ON THE ELECTRET PROPERTIES AND STRUCTURE OF THE PE/HfO_2 POLYMER NANOCOMPOSITE

A.S. HUSEYNOVA
Institute of Physics of the Ministry of Science and Education of the Republic of Azerbaijan, AZ1143, H.Javid ave., 131, Baku city, Republic of Azerbaijan
e-mail:aem05@rambler.ru

The effect of electrothermopolarization (ETP) on the structure and electret properties of polymer nanocomposites based on HDPE and hafnium oxide nanoparticles has been studied. It has been established that the physico-mechanical properties of the PE/HfO_2 nanocomposite improve when 3–10% by weight of HfO_2 nanoparticles is introduced into the PE matrix. The appearance of a long-term electret effect in PE/HfO_2 is associated with the inhomogeneity of the nanocomposite structure and the accumulation of a large number of electric charges at the interface. The interaction between the polymer and nanoparticles has been studied. The results of structural changes occurring in the interfacial zone of the PE/HfO_2 polymer nanocomposite are also presented.

Keywords: nanocomposites, polyethylene, hafnium oxide, polymer nanoparticles, electrothermopolarization,electron microscopy.
PACS: 77.55

1. INTRODUCTION

In recent years, polymer nanocomposites have attracted great interest due to the improvement in the properties of polymers and the expansion of theirapplicationfields. Nanofillers change the supramolecular structure, which largely determines the physicochemical and mechanical properties of the polymer and nanocomposites based on them. The nature of the influence of a nanofiller on the supramolecular structure and properties of polymers is determined simultaneously by the amorphous and crystalline phases, and also plays the role of artificial nuclei for the crystallization of nanoparticles, which leads to a change in the properties of the material [1-6, 10].

It should be noted that, depending on the nature, size, and distribution of nanoadditives, the resulting polymer nanocomposite can be electrically conductive, antistatic, or dielectric. In this regard, the study of the properties of composites obtained by adding metal oxide nanoparticles to polyethylene is of particular interest. The change in the physical properties of polyethylene materials by nanoadditives is mainly due to two reasons: nanoadditive particles act as a source of structuring, and the interfacial layer of the nanoadditive polymer has a large number of charge traps with different activation energies [7–12].

Accordingly, in this work, high-density polyethylene (HDPE) and hafnium oxide nanofiller (HfO_2) were chosen as the polymer matrix, which has improved physical parameters, such as high chemical and thermal stability, and a large band gap (5.5–6 eV), high dielectric constant (22–25), high breakdown strength (3.9–6.7 MV/cm), high neutron absorption coefficient.In technological applications, polymer-based metal-oxide nanoparticles are used in the manufacture of microelectronic circuits, sensors, piezoelectric devices, fuel cells, coatings for surface protectionfrom corrosion, and as catalysts. In the emerging field of nanotechnology, the goal is to create nanocomposites with special properties compared to those of bulk particles.

As it is known, polymers and nanocomposite materials obtained on their basis, after exposure to an external constant electric field at sufficiently high temperatures, are polarized and have electret properties. The main characteristics of the electret material are the magnitude of the electric charge and its stability. They are used in a wide variety of scales, from food processing equipment to special purpose equipment. Physicochemical analyzes of the PE/HfO_2 nanocomposite material were carried out by selecting a special technological mode. The PE/HfO_2 nanocomposite exhibits electrets with a service life that is many times greater than that of pure PE, according to research on their electret properties [13–17].

2. EXPERIMENTAL PART

HDPE polyethylene granules (SOCAR, “Azerikimya” ProductionUnion “Etilen-Polyethylene” plant, 15803-020), CCl_4 organic solvent (Code 141245, 99.5%, CAS Common Chemistry-P.L.C); hafnium oxide (HfO_2) nanoparticles, size 10-20nm, Luoyang Tongrun Info Technology Co., Ltd. China, CAS 12055-23-1, 99%).

Characterization of nanocomposites

SEM analyzes of nanocomposites were made on a JEOL JSM 6610-LV scanning electron microscope at an accelerating voltage of 30 kV.

Polymer nanocomposites were electrothermopolarized (ETP) using an external electric field with a strength of $7\cdot10^6$-$12\cdot10^6$V/m, at a temperature of 373K and then cooling to room temperature for 1 hour. Polymerization provides a strong interaction between the filler and the matrix, which is required in a number of cases. The film thickness is 90–105 μm.

131, H.Javid ave, AZ-1143, Baku
Institute of Physics
E-mail: jophphysics@gmail.com

Synthesis of polymer nanocomposites

PE/HfO_2 polymer nanocomposites were obtained as follows: polyethylene granules were dissolved at room temperature in 60 ml of an organic solvent, carbon tetrachloride (CCl_4), at a temperature of 70C. HfO_2 nanoparticles are added to the polymer solution at various contents and mixed for 5 hours until a homogeneous mixture is obtained. The mixture was transferred to a Petri dish and dried in a vacuum oven for 24 hours. Then, thin films of nanocomposites were obtained from these samples by hot pressing at the melting temperature of polyethylene and a pressure of 15MPa. After hot pressing, the films were cooled in water; the cooling rate of nanocomposite films was 200deg/min.

3. RESULTS AND DISCUSSION

Fig.1 shows the dependences of the surface density of the electret charge (σ) on the lifetime σ=f(τ) for samples of pure PE and nanocomposites based on PE/HfO_2 with different mass content of HfO_2 nanoparticles. It has been established that after ETP, an electret effect is observed in the matrix PE, which is associated with the inclusion of HfO_2 nanoparticles. The lifetime of the surface density of the electret charge for PE and nanocomposites based on PE/HfO_2 was calculated using the following expression:

$$\sigma = \frac{\varepsilon\varepsilon_0 U}{d}$$

where, σ - is the surface charge density, d-is the thickness of the electret, ε-is the permittivity, ε_0-$8.85\cdot10^{-12}$F/m, U- is the charging voltage.

The introduction of HfO_2 nanoparticles can create new traps for electric charge in polyethylene, and this can increase the surface charge density and lifetime. It can be seen that the surface density of electret charges decreases exponentially depending on the lifetime after exposure to discharges. Higher values of σ and relatively higher charge stability is observed for samples of PE/HfO_2 nanocomposites with 5÷10% wt. content of HfO_2 nanoparticles (curve 3, 4, 5). This is due to the presence of deeper traps in the near-surface layers.

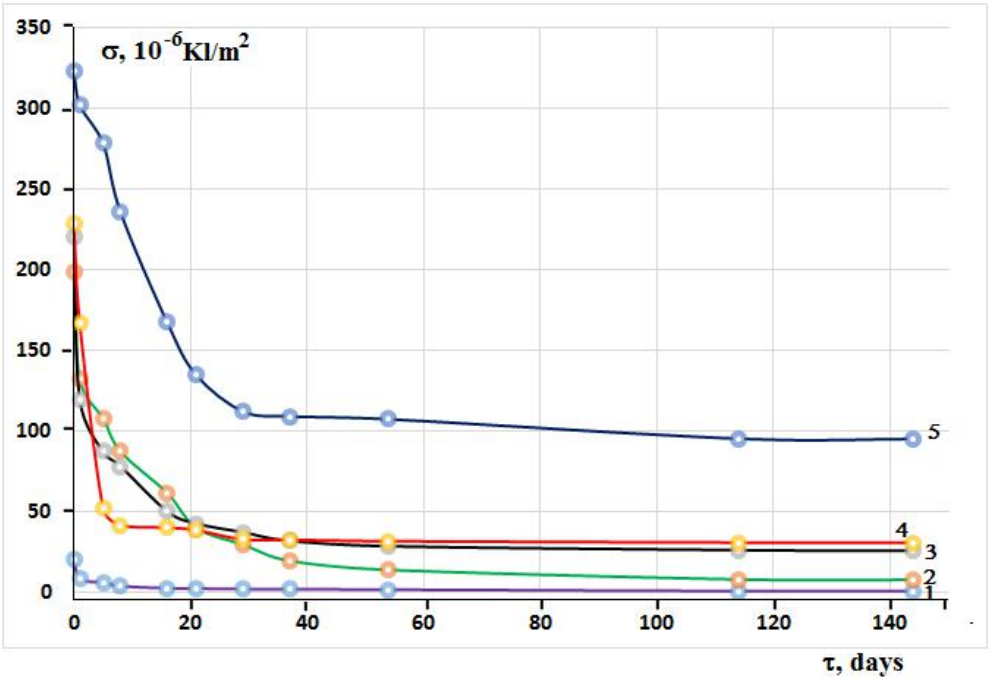

Fig.1. Dependence of the surface density of the electret charge σ on the lifetime τ of compositions: 1. PE; 2. PE/3%HfO_2; 3. PE/5%HfO_2; 4. PE/7%HfO_2; 5.PE/10%HfO_2

In addition, after storage of the electret from a sample of 5÷10wt.%PE/HfO_2 for τ=8÷22 days, the value of σ stabilizes and amounts to $42\div112\cdot10^{-6}$Kl/m^2. This means that the nanocomposite 5÷10wt.%PE/HfO_2 has optimal electret properties. It can also be seen that the surface density of the electret charges of the PE/HfO_2 based nanocomposite is approximately 15 times higher than that of pure polyethylene.

In this work, when studying the electret state, the main attention was paid to the change in the magnitude of the surface charge with time, temperature, and electric field of the ETP, with the structure, relaxation processes of the PE/HfO_2 nanocomposite. The long-term component of the electret effect in PE/HfO_2 is due to in homogeneities of the nanocomposite structure, the boundaries of which are charge traps, which leads to the appearance of Maxwell-Wagner polarization in the entire volume of the nanocomposite.

The change in the electret properties of composites depending on the ETR method is mainly associated with a change in the conditions for stabilization of charges in them and the physical

structure of the matrix. This conclusion correlates well with the results obtained from SEM and electron microscopy (EM) analysis of PE/HfO_2 nanocomposites [17]. Fig.2 shows the EM spectra of PE and a polymer nanocomposite based on PE/HfO_2 depending on the mass content of HfO_2 nanoparticles. Figure 3 shows the SEM spectra of the PE/5%HfO_2 nanocomposite before and after ETP.It should be emphasized that the HfO_2 nanoparticles stabilized with a polyethylene matrix also retained the structural parameters of the nanoparticles contained in the initial dispersion. The study of samples of HfO_2 nanoparticles by electron microscopy (EM) showed that the sample of the dispersion of nanoparticles consists of isotropic nanoparticles. The shape of the particles is uniform, close to spherical.

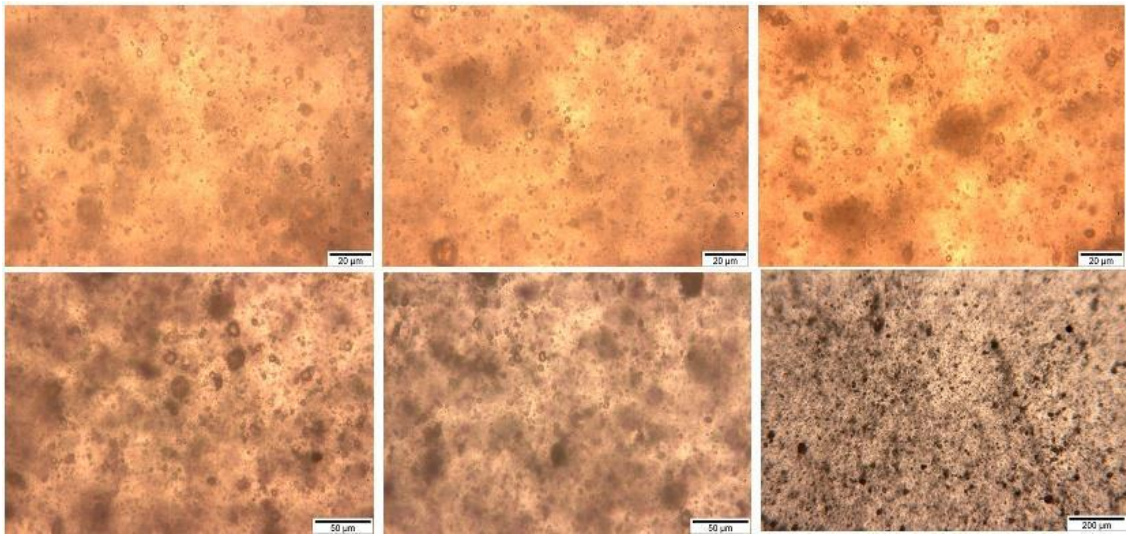

Fig.2. EM images of PE/5%HfO_2 polymer nanocompositesş

Analysis of the EM of the nanoparticles showed that the nanoparticles are uniformly distributed over the volumestabilizing matrix and isolated from each other.

The morphology of the samples and the distribution of HfO_2 nanoparticles in the volume of the polymer matrix were studied using a scanning electron microscope (SEM) (Fig. 3). Elemental analysis in the EMF spectrum also shows (Fig. 3.b) that the resulting nanoparticles are hafnium nanoparticles. Fine crystalline particles can be observed on the surface of Figure 3a. Based on the SEM images, it can be said that the HfO_2 nanoparticles are evenly distributed and aggregated on the surface of the polymer matrix. The average size of iron nanoparticles stabilized in the presence ofpolyethylene is 4,93 nm. Elemental analysis in the EMF spectrum also shows that the obtained nanoparticles are hafnium nanoparticles.

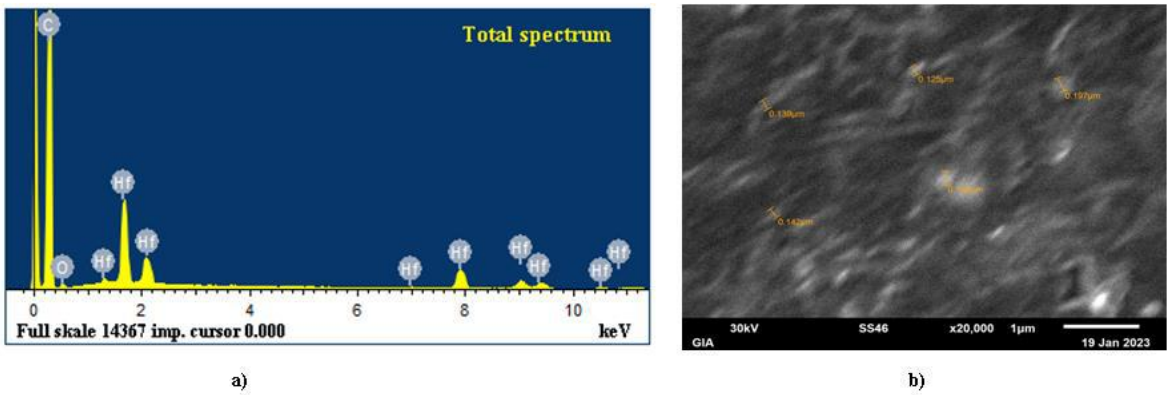

a) b)

Fig.3. SEM images of PE/5%HfO_2 polymer nanocompositesş

RESULTS

Thus, the PE/HfO_2 polymer nanocomposites developed by us represent a new, promising class of electret materials that will undoubtedly be in demand in modern science-intensive technologies. It has been established that with the introduction of 3-10% amounts of HfO_2, the physical and mechanical properties of the PE/HfO_2nanocomposite increase, and the performance of PE products increases.

According to the data of electron and SEM microscopy, in all samples, the nanoparticles are spherical, isolated from each other, and uniformly distributed over the volume of the polyethylene matrix.

[1] *T. Xu Fengting, M. Thaler Sean, A. Lopez Carlosk, A. Barnard John, Butera Alejandro, L. Weston James.* Appl.Phys.Lett., 2005, t.86, №7, p.456.

[2] *G.A. Mekishev, T.A. Yovcheva, E.A. Gentcheva, S.R. Nedev.* Study of electrets stored of pressures lower than atmospheric. J. Electrostatics, 2005, t.63, №11, p.1009-1015.

[3] *L. Zhu.* Exploring strategies for high dielectric constant and low loss polymerdielectrics, J. Phys. Chem. Lett. 5(21) (2014) 3677-3687.

[4] *Z.M. Dang, J. Yuan, J. Zha, T. Zhou, S. Li, G. Hu.* Fundamentals, processes andapplications of high-permittivity polymer–matrix composites, Prog. Mater. Sci. 57(4)(2012) 60-723.

[5] *A. Gulyakova, P. Frübing, and Yu.A. Gorokhovatskiy*. Relaxation processes in high-impact polystyrene films withtitanium dioxide inclusions. Conf. Proc. of XIII Int. conf."Physics of Dielectrics", St. Petersburg, 23-26 May, vol.2, pp.C.56-59, 2011.

[6] *Diaa-Eldin A. Mansour, Nagat M. K. Abdel-Gawad, Adel Z. El Dein, Hanaa M. Ahmed, Mohamed M. F. Darwish and MattiLehtonen.* Recent Advances in Polymer Nanocomposites Based onPolyethylene and Polyvinylchloride for Power Cables. Materials 2021, 14, 66.

[7] *Jalal Azadmanjiri, Christopher C. Berndt, James Wang, Ajay Kapoor, Vijay K. Srivastava, Cuie Wen.* A Review on Hybrid Nanolaminate Materials Synthesized by DepositionTechnique for Energy Storage Applications. Journal of Materials Chemistry A, p.1-39.

[8] *Sheng Chen, Yang Zhou, Hang Luo,Lin Tang, Ru Guo, Dou Zhang.* Core-shell TiO2@HfO2 Nanowire Arrays with Designable Shell Thicknesses for Improved Permittivity and Energy Density in Polymer Nanocomposites.Composites: Part A (2020),Applied Science and Manufacturing, Volume 137, October 2020, 106012.

[9] *G. Wang, Y. Huang, Y. Wang, P. Jiang, X. Huang.* Substantial enhancement of energy storage capability in polymer nanocomposites by encapsulation of $BaTiO_3$ NWs with variable shell thickness. Phys. Chem. Chem. Phys. 2017, 19(31):21058-21068.

[10] *G.D. Wilk, R.M. Wallance and J.M. Anthony.* J. Appl. Phys., 2001, 89, 5243-5275.

[11] *R. M. Wallace and G. Wilk.* MRS Bul., 2002, 27, 192-197.

[12] *H. Zhang, W. Guo, Y. Yu, B. Li, C. Wu.* Structure and properties of compatibilized recycled poly (ethylene terephthalate)/linear low density polyethylene blends. Eur. Polym. J. 2007, 43, 3662–3670.

[13] *A. Maniadi, M. Vamvakaki, M. Suchea, I.V. Tudose, Popescu, M.; Romanitan, C.; Pachiu, C.; Ionescu, O.N.; Viskadourakis, Z.; Kenanakis, G.; et al.* Effect of graphene nanoplatelets on the structure, the morphology, and the dielectric behavior of low-density polyethylene nanocomposites. Materials 2020, 13, 4776.

[14] *M.M. Habashy, A.M. Abd-Elhady, R.A. Elsad, M.A. Izzularab.* Performance of PVC/SiO_2 nanocomposites under thermal ageing. Appl. Nanosci. 2019, 1–9.

[15] *K. Kukli, M. Ritala, M. Leskela. J. Electrochem. Soc.*, 2001, 148, F35-F41.

[16] *D. Ai, H. Li, Y. Zhou, L. Ren, Z. Han, B. Yao, W. Zhou, L. Zhao, J. Xu, Q. Wang.* Tuning nanofillers in in situ prepared polyimide nanocomposites for high-temperature capacitive energy storage, Adv. Energy Mater. 10(16) (2020) 1903881.

[17] *C. Chen, Y. Xie, J. Liu, J. Li, X. Wei, Z. Zhang.* Enhanced energy storage capability of P(VDF-HFP) nanodielectrics by HfO_2 passivation layer: preparation, performance and simulation, Compos. Sci. Technol. 188 (2020) 107968.

Received: 05.09.2023

STUDY OF THE STABILITY OF THE ELECTRET STATE IN A NANOCOMPOSITE POLYMER FILM BASED ON POLYETHYLENE WITH A NANOPARTICLE Ta_2O_5

A.S. HUSEYNOVA[1], M.N. BAYRAMOV[2], F.F. YAHYAYEV[1]

[1]Institute of Physics of the Ministry of Science and Education of the Republic of Azerbaijan, AZ 1143, H. Javid ave., 131, Baku city, Republic of Azerbaijan,e-mail:aem05@rambler.ru

[2]Institute of Radiation Problems of the Ministry of Science and Education of the Republic of Azerbaijan, AZ 1143, B. Vahabzade str., 9, Baku city, Republic of Azerbaijan

Have studied the electret properties of polymer nanocomposites based on PE and tantalum oxide nanoparticles. At a nanoparticle concentration of between 7% - 10%, it is possible for the electret properties of PE/Ta_2O_5 polymer nanocomposites to change significantly. The results of structural changes of polymer nanocomposite PE/Ta_2O_5 in its volume and interphase zone are also presented.

Keywords: nanocomposites, polyethylene, tantalum oxide, polymer nanoparticles, electrothermopolarization.
PACS: 77.55

INTRODUCTION

The creation of nanocomposite polymer materials with an improved complex of properties is a major direction in the physics, chemistry and technology of polymers. This task can be solved, for example, by modifying the surface of the polymer by various methods, which is essential for controlling its dielectric properties, or by adding various dispersed nanofillers to the volume of the polymer.Using numerous methods of modification of polymers, it is possible to improve, in particular, their electrophysical and adhesive characteristics [1-3].

The study of electrophysical properties of nanocomposite polymer films is an actual problem of condensed state physics. Currently, the mechanical properties of nanocomposites have been studied in detail, which is explained by their active use as construction materials. At the same time, there are no systematic studies of the electrophysical properties of nanocomposite films, although materials based on them are used both in the manufacture of electroacoustic and electromechanical signal converters, dosimeters,pressure sensors, air filters, and when solving a number of applied problems.

In this work, high-density polyethylene (HDPE) and tantalum nanooxide (Ta_2O_5) were chosen as the polymer matrix. At present, there are practically no models that help to reveal the mechanisms of the influence of nanofillers on the electret properties of composite polymer films and the regularities of the relaxation processes occurring in them. In this regard, the study of charge relaxation processes in composite films based on HDPE with the addition of a nanofiller (tantalum dioxide) is an urgent task of scientific and practical interest. The mechanisms and parameters of electrical relaxation processes in nanocomposite polymer films based on HDPE with nanofiller (tantalum dioxide) were determined to clarify the nature of the electret state in these films, as well as the factors limiting the stability of the electret state [6,7,9,10].

Literature data on the study of the electret state in nanocomposite HDPE films with tantalum dioxide inclusions are practically absent. In this regard, the study of the electret properties of nanocomposite materials based on HDPE remains an urgent problem in condensed matter physics.

EXPERIMENTAL PART

Materials: HDPE polyethylene granules (SOCAR, “Azerikimya” ProductionUnion “Etilen-Polyethylene” plant, 15803-020), CCl4 organic solvent (Code 141245, 99.5%, Cas No-[56-23-5], Common Chemistry- P.L.C); tantalum oxide nanoparticles (Ta_2O_5), (Hongwu International Group, Ltd, China, size 100-200nm, 99.9%, T502).

PE/Ta_2O_5 polymer nanocomposites were obtained as follows: polyethylene granules were dissolved at room temperature in 60 ml of an organic solvent, carbon tetrachloride (CCl_4), at a temperature of 70°C. Ta_2O_5 nanoparticles were added to the polymer solution at various volume concentrations and mixed for 5 hours until a homogeneous mixture was obtained. The mixture was transferred to a Petri dish and dried in a vacuum oven for 24 hours. Then, thin films of nanocomposites were obtained from these samples by hot pressing at the melting temperature of polyethylene and a pressure of 15 MPa. After hot pressing, the films were cooled in water; the cooling rate of the nanocomposite films was 200 deg/min.

X-ray phase studies of nanocomposites were performed on a D2 Phaser X-ray diffractometer in reflection mode (Bragg-Brentano geometry) using CuKa radiation (average wavelength λ=1.5406 Å, nickel β-filter). Registration was carried out in a continuous mode in the range of angles 2θ = 5–80°.

Polymer nanocomposites were electrothermopolarized (ETP) using an external electric field with a strength of $7\cdot10^6$-$12\cdot10^6$V/m, at a temperature of 373K and then cooling to room temperature for 1 hour. The film thickness is 95–100

131, H.Javid ave, AZ-1143, Baku
Institute of Physics
E-mail: jophphysics@gmail.com

μm. The electret characteristics were measured with an EFPM-1 device.

RESULTS AND DISCUSSION

To establish the effect of the content of nanoparticles on the structure of nanocomposites, XRD analyzes were used [8].

On fig. Fig.1 shows X-ray diffraction patterns of PE and nanocomposites based on PE/wt.%Ta_2O_5. On the diffraction patterns of the modified PE/3-7 wt.% Ta_2O_5 nanocomposite at 2θ: PE/3wt.%Ta_2O_5- 25,2° (446), 36,9° (248), 47,5° (180), 55,3° (124); PE/5wt.%Ta_2O_5-25,2° (464), 36,9° (277), 47,5° (163), 55,3° (151); and PE/7wt.%Ta_2O_5- 25,2° (505), 36,9° (288), 47,5° (164), 55,3° (152) peaks corresponding to Ta_2O_5 nanoparticles are observed. It can also be seen from the diffraction patterns that the intensity of the peak at 2θ: 24,5°(740), 38,2° (204) and 40,8°(229) in the PE matrix is observed, which indicates an increase in the semi-crystallinity degree of the matrix.

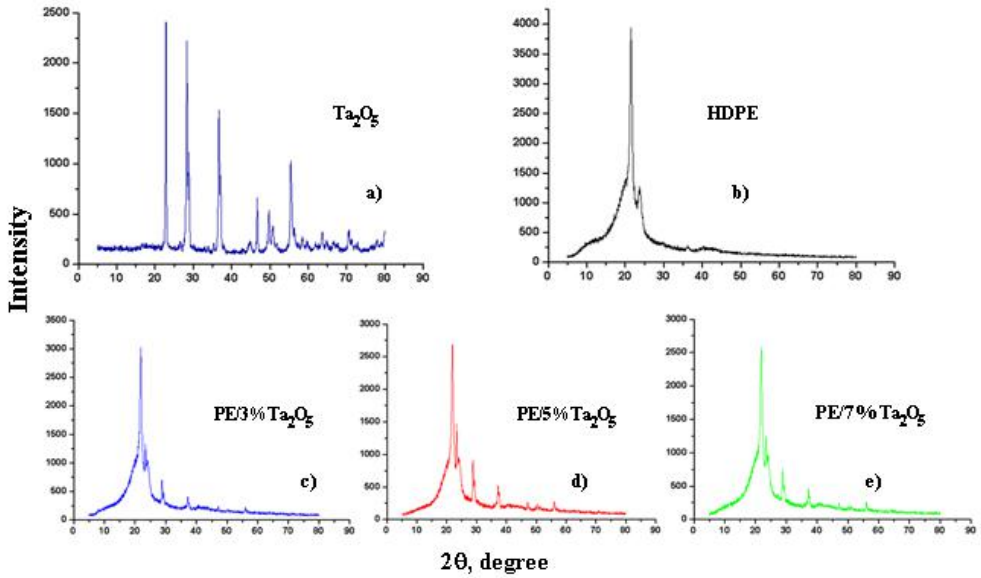

Fig. 2. XRD pattern of PE and PE/Ta_2O_5 based nanocomposites: a) Nanoparticles Ta_2O_5; b) PE; c) PE/3%Ta_2O_5; d) PE/5%Ta_2O_5; e) PE/7%Ta_2O_5

At the first stage, we analyzed the effect of the polymer structure, which can be changed within certain limits during processing, on its electret properties. This can lead to an increase in surface density and charge carrier lifetime. To investigate the effects of structure factors and structural relaxations on electret-effect type processes, we chose HDPE, a classical crystallizing polymer. It should be noted that stable electrets can be obtained from HDPE. The dependence of the surface density of the electret charge (σ) on the lifetime (τ) in PE/Ta_2O_5 nanocomposites has been determined. The surface density of the electret charge depending on the lifetime for nanocomposites based on PE/$Ta_2O_5$was calculated using the following expression:

$$\sigma = \frac{\varepsilon\varepsilon_0 U}{d}$$

where, σ is the surface charge density, d is the thickness of the electret, ε is the permittivity of the sample, ε_0-$8.85\cdot10^{-12}$F/m, U is the charging voltage.

The dependence of the electret properties of PE and PE/Ta_2O_5 on the lifetime is shown in Fig.1. Polymerization provides a strong interaction between the filler and the matrix, which is required in a number of cases. It can be seen that the inclusion of the Ta_2O_5 nanofiller in the polymer matrix contributes to the creation of deep traps for charge carriers and enhancescharge stability in nanocomposite films. The resulting nanocomposites with 5-10wt.%Ta_2O_5 content have optimal electret properties. It is shown that the surface density and lifetime of electret charges studied by the inductive method increase in nanocomposites based on PE/wt.%Ta_2O_5. The Ta_2O_5 nanofiller in the polyethylene matrix can create traps for new electric charges in it.

Samples of 5÷10% PE/Ta_2O_5 have higher charge stability σ (curve 3, 4, 5). This is due to the presence of deeper traps in the near-surface layers. As can be seen from Fig.1, for samples at the initial stage with lifetime values up to 6÷10days, the value of σ is characterized by an exponential decrease σ=f(τ), and then a linear decrease in σ (10÷19 days). Comparison of σ in the stable section of dependences σ= f(τ) for different samples shows that samples based on 5÷10 wt.% PE/Ta_2O_5 have optimal electret properties, and the value of the surface charge density stabilizes and amounts to $37\div92\times10^{-6}$Kl/m^2. The changes in the electret properties of PE and PE/wt%Ta_2O_5 according to the supramolecular structure (SMS) of the nanocomposites are related to the charge-stabilizing features in different parts of the structural elements and, accordingly, with the depth of traps in the polymer.

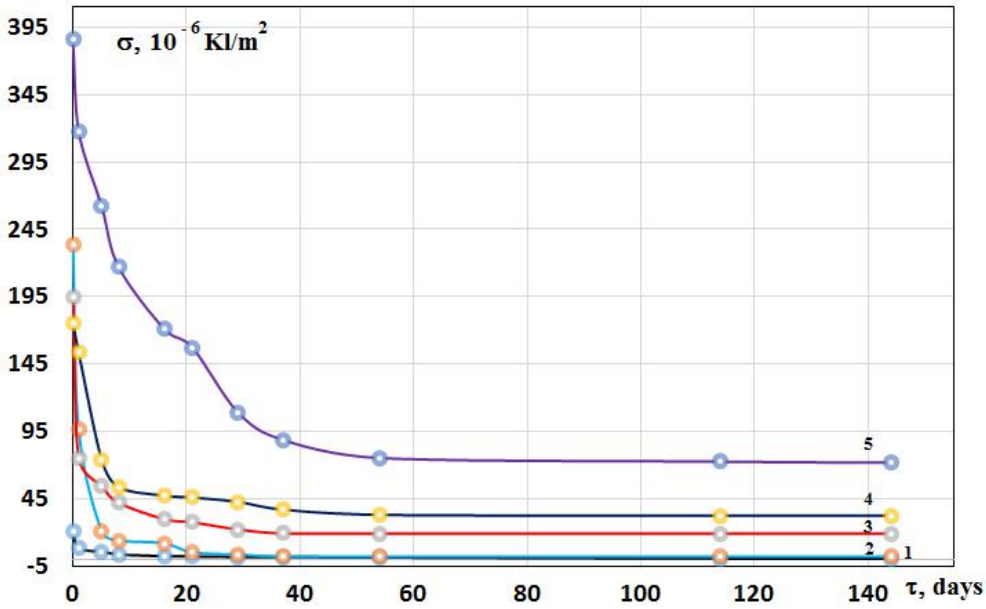

Fig.2. The dependence of the surface density of the electret charge σ on the lifetime of the compositions: 1. PE; 2.PE/3%Ta_2O_5; 3. PE/5%Ta_2O_5; 4. PE/7%Ta_2O_5; 5. PE/10%Ta_2O_5

It is also seen that σ for nanocomposites based on PE/wt%Ta_2O_5 is approximately 17,5 times greater than for pure PE. The nature of the electret properties of the studied systems is similar to each other depending on the mass content of the filler. It can be said that the chemical nature of fillers in improving the electret properties is significant in comparison with the contribution of their structural parameters (specific area and surface area). According to G. Sessler, Borisova M. E., Lushcheikin G. A [4,5], the interface between the amorphous and crystalline phases acts as traps for charge carriers, therefore, it can be the main reason for the significant difference in the electret properties of nanocomposites obtained by the induction method.

FINDINGS

It has been established that the stability of the electret state in composite polymer films based on HDPE with inclusions of tantalum dioxide is significantly higher compared to the original films without filler. And this makes it possible to consider nanocomposite films based on it as a promising material for the creation of electroacoustic and electromechanical transducers. It is shown that the stability of the electret state in nanocomposite HDPE polymer films depends nonmonotonically on the volume concentration of nanofillersin the sample. The optimal volume concentration of tantalum dioxide, which provides the highest stability of the electret state in HDPE films, has been determined. Two conclusions can be drawn from the discussion mentioned above. First, nanofillers play an important role in the polarization of nanocomposites and are capable of changing the polarization intensity of intrinsic dipoles in polymers. Second, the trap depth can also be changed by introducing nanofillers and, consequently, the interfacial polarization in nanocomposites can be changed. The influence of the nanofilling process on the formation of electret properties and on the process of stabilization of electret charges can be explained from the point of view of modern ideas about the structure of the PE crystallization mechanism.

[1] *Heh-Chang Huang, Tsung-Eong Hsieh.* Preparation and Characterizations of Tantalum Pentoxide (Ta_2O_5) Nanoparticles and UV-Curable Ta_2O_5-Acrylic Nanocomposites. Journal of Applied Polymer Science, Vol. 117, p.1252–1259 (2010) VC 2010 Wiley Periodicals, Inc.

[2] *J.I. Hong, P. Winberg, L.S. Schadler.* Mater Lett 2005, 59, 473.

[3] *S.D. Cho, J.Y. Lee, J.G. Hyun, K.W. Paik.* Mater SciEng B 2004, 110, 233.

[4] *T.I. Yang, P. Kofinas.* Polymer 2007, 48, 791.

[5] *Yu.A. Gorokhovatsky*. Relaxation of the electret state in polyethylene-based polymeric fiber // Materials of the X International Conference "Physics of Dielectrics". SPb: Publishing house RSPU m.A.I. Herzen.2004.p.84-86.

[6] *M.A. Ramazanov, A.S. Quseynova, F.V. Hajiyeva.* Influence of temperature and time regimes of crystallization and electrothermopolarization on the physical structures of polypropylene and MnO_2-based composition Journal Optoelectronics and Advanced Materials. –, Rapid Communications v.3 №11- 2009, p.1204-1206.

[7] *M.A. Ramazanov, A.S. Quseynova.* Influence of polarization processes on the charge states and dielectric properties of polyethylene-based

compositions with low-molecular additions PE+$PbCrO_4$ and PE+Cr Optoelectronics and Advanced Materials – Rapid Communications v. 7, №. 9-10, 2013, p.78

[8] *B.D. Cullity, S.R. Stock.* Elements of X-Ray Diffraction, 3rd ed.; Prentice Hall: Upper Saddle River, NJ, 2001.

[9] *D.A. Rychkov.* Stabilization of the charge of polymer electrets: monograph / SPb. Publishing house of the Russian State Pedagogical University im. A.I. Herzen, 2013.p.159.

[10] *A. Gulyakova, P. Frübing, and Yu.A. Gorokhovatskiy*. Relaxation processes in high-impact polystyrene films with titanium dioxide inclusions // Conf. Proc. of XIII Int. conf. "Physics of Dielectrics", St. Petersburg, 23-26 May, vol.2, pp. C.56-59 (2011).

Received: 05.09.2023

STUDY OF LOCAL STRUCTURE Se–As GLASSY SEMICONDUCTOR SYSTEM AND THE MECHANISM OF CURRENT PASSAGE THROUGH THE Al-$Se_{95}As_5$<EuF_3>-Te STRUCTURE

S.N. GARIBOVA

Institute of Physics named after G.M. Abdullayev of Ministry of Science and Education, AZ-1143, Baku, H. Javid ave. 131

Khazar University, Department of Physics and Electronics, 41 Mehseti Str., Az-1096, Baku, Azerbaijan

The local structure features of $Se_{95}As_5$ chalcogenide glassy semiconductor doped with EuF_3 rare-earth impurity and the mechanism of current passage through Al– $Se_{95}As_5$<EuF_3>–Te structure have been investigated by the X-ray, Raman micro-spectroscopy methods and current-voltage characteristics. The basic structural elements and chemical bonds formed the amorphous matrix, and the features of current flow in strong electric fields through the Al– $Se_{95}As_5$<EuF_3>–Te structure in two directions of the applied electric field have been determined.

Keywords: conductivity, amorphous structure, x-ray diffraction, Raman spectroscopy.
PACS: 61.43.Dq, 72.10.D

1. INTRODUCTION

A strong increase in the number of works devoted to studies of the structure and electronic properties of chalcogenide glassy semiconductor (CGS) materials is due to the wide scope of their application and the emergence of new applications over time. In particular, CGS materials are widely used as active media in lasers, optical amplifiers and converters, and are considered promising materials for memory elements, recording information carried out due to the glass-crystal phase transition caused by an electric field. However, the success of applied tasks depends on the ability to control and manage electronic properties. It is known that the electronic properties of CGSs are closely related to the features of the local structure on a short- and medium-order range. The study shows that the local structure can be directionally changed by changing the chemical composition and alloying [1].

2. CONTENT

The present work is devoted to the study of the local structure of the $Se_{95}As_5$ glassy semiconductor containing of EuF_3 impurity and the mechanism of current flow through Al-$Se_{95}As_5$<EuF_3>-Te structure. The choice of the object is due to the fact that amorphous selenium with the addition of arsenic as a resistant material to crystallization is considered more promising for use than amorphous selenium with better photoelectric parameters, but easily crystallizing. However, the addition of arsenic to selenium affects the photoelectric properties. It is known that the electronic and photoelectric properties of CGS (selenium with arsenic addition also belongs to this class of materials) is controlled by the centers of effective correlation energy (U^- -centers) manifesting themselves in the form of charged defects (D^+ and D^-), the concentration of which can be changed by introducing impurities manifesting in the form of charged centers [2]. It is considered that the EuF_3 impurity of should contribute to the manifestation of positive europium ions, which will lead to a change in the concentration of intrinsic charged defects, also Eu^{3+} and F^- as are chemically active elements, formed bonds between selenium and arsenic atoms will cause a change in the amorphous matrix. These factors will affect the electronic and photoelectric properties of the investigated material [3].

3. RESULTS AND DISCUSSION

X-ray diffraction patterns shown in Fig. 1 of two bands indicate amorphous films. In addition, the diffraction pattern contains a peak, the so-called first sharp diffraction peak (FSDP), the presence of which is associated with the existence of ordering in the arrangement of structural elements outside the region of the first coordination sphere and is called the middle-region-order (MRO). Within the framework of the Elliot void-cluster model, using the FSDP parameters, the correlation length and the "quasiperiod" of atoms density fluctuations in the MRO, also the diameter of the nanovoids, have been estimated. It was shown that the EuF_3 impurity mainly affects the values of the R "quasiperiod" and D diameter of the nanovoids.

The Raman spectrum of amorphous selenium consists of a broad maximum at a frequency of 254 cm^{-1} and a narrow maximum at 237.8 cm^{-1} corresponding to vibrations of the Se_8 ring molecules and - Se-Se- chain molecules (Fig. 2a). Adding arsenic to amorphous selenium leads to a significant change in its Raman spectrum (curve 1, Fig. 2b). The peak at 254 cm^{-1} is noticeably attenuated, which is associated with the rupture of part of the ring molecules. The appearance of peaks in the frequency range 209÷220 cm^{-1} is associated with the formation of various molecular fragments (for example, As_4Se_4 type). A peak at 225 cm^{-1} is also observed in all CGS systems containing As and Se atoms and is attributed to the pyramidal structural elements of $AsSe_3$.

131, H.Javid ave, AZ-1143, Baku
Institute of Physics
E-mail: jophphysics@gmail.com

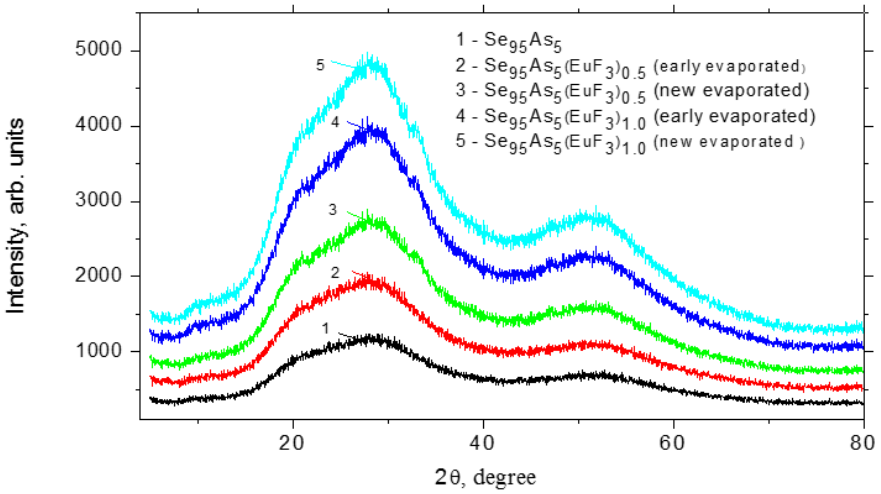

Fig.1. X-ray diffraction patterns of CGS films.

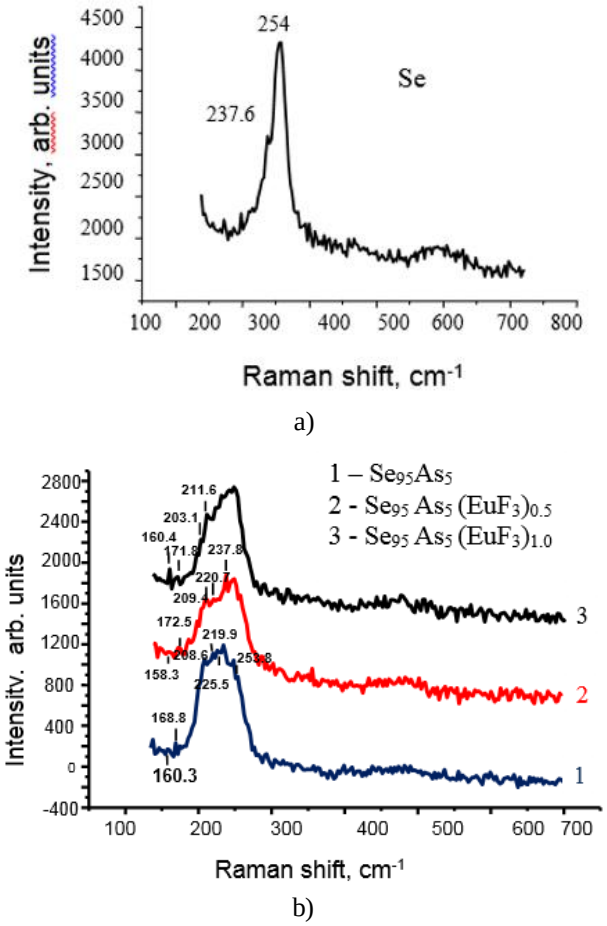

Fig.2. Raman spectra of the Se (a) and Se-As, Se-As-EuF_3 (b) films.

The weak maximum at 168.8÷172 cm^{-1} observed in all spectra (Fig. 2b) is attributed to vibrations of the As-As homopolar bond.

An investigation of the current–voltage (I–V) characteristics of the Al– $Se_{95}As_5$<EuF_3>–Te structure (Fig. 3) showed that the current flow in it when a positive potential is applied to Te electrode is carried out by the mechanism of monopolar injection currents limited by the space charge (Fig. 3a), and with reverse polarity, an N-type I-V characteristic have been observed (Fig. 3b).

The I-V characteristic at a positive potential in the tellurium electrode (Fig.3a) begins with an ohmic law with an increase in the applied voltage and passes into the region corresponding to a power law, i.e. $I \sim V^n$, where n exceeds the value 2. Next, the section is observed where $I \sim V^2$. Finally, the quadratic region is replaced by the region where the increase in current with voltage is described by a close exponential dependence, which is usually associated with the ionization of local centers [4].

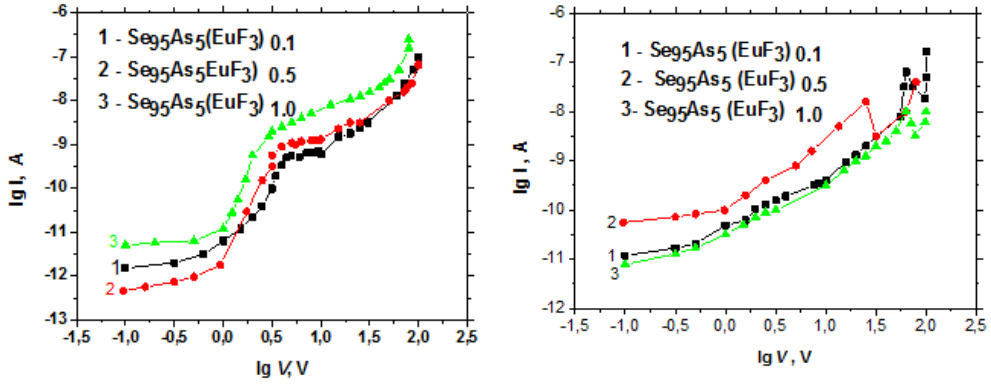

a) b)

Fig. 3. The I – V characteristics of the Al– $Se_{95}As_5$<EuF_3>–Te structure upon application of positive (a) and negative (b) potentials to Te at room temperature: 1- $Se_{95}As_5$ (EuF_3), 2-$Se_{95}As_5$(EuF_3).

With a negative potential at the tellurium electrode, with increasing applied voltage, the linear dependence is replaced by a nonlinear law, and finally, at electric field intensities exceeding 10^5 V/cm, an N-shaped I-V characteristic is observed (Fig.3b).

This behavior of the I–V characteristics of CGSs in strong electric fields was associated with tunneling ionization of the U^- - centers [5].The essence of this model is that, at the first stage of the process, the electron is thermally excited to a certain energy level, then the excited electrons tunnel through the potential barrier created by the electric field of the D center during ionization of the D^0 center, or by the short-range field of the neutral D^0 center at ionization of the D^- center. According to [6], in a strong electric field, ionization of neutral and negatively charged U^- - centers occurs, also the processes electron capture by ionized centers:

$$D^- \leftrightarrow D^0 + e,$$

$$D^0 \leftrightarrow D^+ + e.$$

The decrease in current is apparently due to the fact that after reaching a certain concentration of free charges carriers, they are avalanche-like by U^- - centers, or the recombination of electrons and holes. The absence of an N-shaped region in the current-voltage characteristic upon application of a positive potential to the tellurium electrode is explained by the fact that strong injection of charge carriers through the contacts prevails over capture and recombination processes.

4. CONCLUSION

Using the theory of injection currents and the mechanism of current flow through amorphous chalcogenide films at strong electric fields proposed by the authors of [7], the energy position and concentration of local centers have been determined, the ionization of which leads to an exponential increase in current strength.It was shown that low concentrations of EuF_3impurities (up to 0.1 at%) decrease the concentration of these centers, and high (more than 0.1 at%) increase them. The behavior of EuF_3 impurities in low concentrations is explained by the chemical activity of REE and fluorine ions, which can form chemical compounds with selenium and arsenic, as a result of which the concentration of the original intrinsic defects decreases. The behavior of EuF_3 impurities in high concentrations occurs according to the model of charged intrinsic defects [8]. If we assume that rare-earth element impurities mainly manifest themselves in the form of positively charged ions, as a result, their presence should provide a decrease in the concentration of D^+ centers, and the concentration of D^- - centers should increase, which was established experimentally.

[1] *R.I. Alekberov, A.I. Isayev, S.I. Mekhtiyeva, M. Fábián*, J. Non-Cryst.Sol., 470, p. 152-159,2017.
[2] *L.P. Kazakova, E.A. Lebedev, N.B. Zakharova, I.I. Yatlinko, A.I. Assayed, S.I. Mekhtiyeva*, J. Non-Cryst.Sol., 167, p. 65- 69, 1994.
[3] *A.I. Isayev, S.I. Mekhtiyeva, S.N. Garibova, V.Z. Zeynalov*, Semiconductor, 48, issue 2, p.148-151, 2014.
[4] *E. Voronkov*, J. Non - Cryst. Sol., 353, p. 259-2594, 2007.
[5] *V.N. Abakumov, V. Karpus, V.I. Pepel, I.N. Yassiyevich*, FTP, 22, p. 262-268, 1988. (in Russian).
[6] *N.A. Boqoslovskiy, K.D. Tsendin*, FTP, 43, p.1378-1382, 2009. (in Russian).
[7] *E.N. Voronkov, S.A. Kozyukhin*, FTP, 43, p. 953-956, 2009. (in Russian).
[8] *D. Adler, M.S. Shur, M. Silver, S.R. Ovshinsky*, J.Appl. Phys., 51, p. 3289- 3309, 1980.

Received: 07.09.2023

EFFECT γ- RADIATION ON THE ELECTRICAL PROPERTIES OF $In_{0.999}Ag_{0.001}Se$ SINGLE CRYSTALS

G.I. ISAKOV, A.A. ISMAYILOV*, A.A. ISMAYILOV
Ministry of Science and Education of Azerbaijan Institute of Physics named after academician H.B. Abdullayev, Baku-1143, H. Javid Ave. 131
gudart.isakov@gmail.com
**Azerbaijan Technical University, Baku-1073, H. Javid avenue 25*

It was determined that when $In_{0.999}Ag_{0.001}Se$ crystals are irradiated with 50 krad dose γ-quanta, centers with a depth of 0.17 eV are formed in the forbidden band. Before irradiation, in the prohibited band there are uncontrollable centers with the location depth Ev + 0.1 eV. Centers resulting from irradiation compensate for uncontrolled Ev +0.1eV centers. With this, the concentration of charge carriers and electrical conductivity decreases. As the radiation dose increases, new centers are not formed, the concentration of previous centers increases. The difference between the electrical conductivity of unirradiated and radiated crystals also increases with decreasing temperature.

Keywords : γ-quanta , irradiated crystals, perfect crystals, industrial electronics, chalcogenides, perfection of crystals due to radiation.
PACS: Nr.71.20Semiconductor compounds; 72.20.Fr Shipping and handling in low areas.

INTRODUCTION

InSe belongs to the group of $A^{III}B^{VI}$ layered crystals. Despite having high defectivity, these crystals are used in the production of various devices in industrial electronics, solar cells [1,2], optical modulators [3,4], X-ray radiation detectors [5,6], radioactive measuring devices in nuclear reactors [7], pressure transmitters [8] are used in preparation.

Various effects are used to control the physical properties of these crystals. In the current study, different doses of γ-radiation were used as an external effect.

Semiconductors are irradiated with high-energy particles, changes in their crystal structure occur. This affects the physical properties of crystals. Since the effect of radiation on different crystals is different [7, 9, 10,11], the nature of radiation, kinetics and stability of their formation during the interaction of high-energy particles with solid bodies have been studied. In layered semiconductors, like most semiconductor materials, electrical conductivity changes significantly depending on the radiation dose during interaction with γ-quanta [12,13].

Purpose of conducting experiments; Irradiated with doses of 50 and 100 krad consists of determining the temperature dependence of the electrical conductivity of $In_{0.999}Ag_{0.001}Se$ crystals, the depth of the centers formed depending on the radiation dose, and the temperature dependence of the relative change of their electrical conductivity.

DISCUSSION OF EXPERIMENT AND RESULTS

In InSe, the coordination number of In atoms is 4, and the coordination number of Se atoms is 3. Accordingly, a 4-coordinated In atom forms a tetrahedral bond with a 3 - coordinated Se atom, and 1 In atom hybridizes at the sp^3 level [14,15]. The above allows us to conclude that the nature of the chemical relationship between indium and silver monoselenides is similar, and to determine the formation of solid solutions between InSe and AgSe.

In this study, homogeneous $In_{0.999}Ag_{0.001}Se$ samples were taken to study the electrophysical properties. For this purpose, In-In 000, Se B-3 and Ag-999.9 branded elements were used. Chemical elements In, Ag, Se were chopped and filled into a quartz ampoule, air was sucked up to a pressure of 10^{-4} Pa. For this, the direct synthesis method was used. Single crystals of $In_{0.999}Ag_{0.001}Se$ were grown by the vertical Bridgman method. The speed of movement of the ampoule in the oven was 0.3 cm/h. The resulting crystals were studied by differential thermal analysis (DTA), X-ray phase analysis (RFA) and microhardness measurements. Silver paste was used as ohmic contacts. The contacts are placed opposite the opposite surfaces of the samples. The sample is made in the form of a parallelepiped and the size shown below is 10x4x2mm^3 . The samples were irradiated with a Co^{60} source (direct-acting radiation chemical unit) РХУНД-20000 with an γenergy of 1.25 MeV, a flux density of $1.4 \cdot 10^{11}$ quant/s ·cm ^{2} and a radiation power of ~ 50 rad/s in the radiation zone at room temperature· radiation doses of -quanta 0; 50; and was 100 krad. Samples for the experiment were placed in a special cryostat. The temperature of the samples was measured by a chromel-alumel thermocouple located on their surface. It was determined that $In_{0.999}Ag_{0.001}Se$ solid solutions have n-type conductivity according to the sign of thermo-eq. The electrical conductivity of $In_{0.999}Ag_{0.001}Se$ samples in the temperature range of 142-294K was measured in a constant electric field. First, the temperature dependence of the electrical conductivity of the non-irradiated crystal was measured. Then, the temperature dependence of the electrical conductivity of crystals made of $In_{0.999}Ag_{0.001}Se$ crystals irradiated with 50 and 100 krad dose γquantums was measured. Based on the

131, H.Javid ave, AZ-1143, Baku
Institute of Physics
E-mail: jophphysics@gmail.com

results obtained from the experiment, the temperature dependence of electrical conductivity before and after irradiation was established in Arrenus coordinates, and for both cases, the location depth of the centers located in the forbidden zone was calculated. When the sample is irradiated with a dose of 50 krad, the electrical conductivity decreases compared to the non-irradiated sample. This is because when the crystal is irradiated with a dose of 50 krad, radiation centers with a depth of 0.17 eV are formed. The electrical conductivity decreases because the uncontrolled defect centers with a depth of 0.1 eV are compensated by the radiation induced defect centers. As a result, the concentration of charge carriers decreases. As the radiation dose increases, new centers are not formed, the concentration of previous centers increases. The dependence of electrical conductivity on the radiation dose V_{In} occurs with the accumulation of acceptor defects. Experimental results of this phenomenon are shown in figure 1.

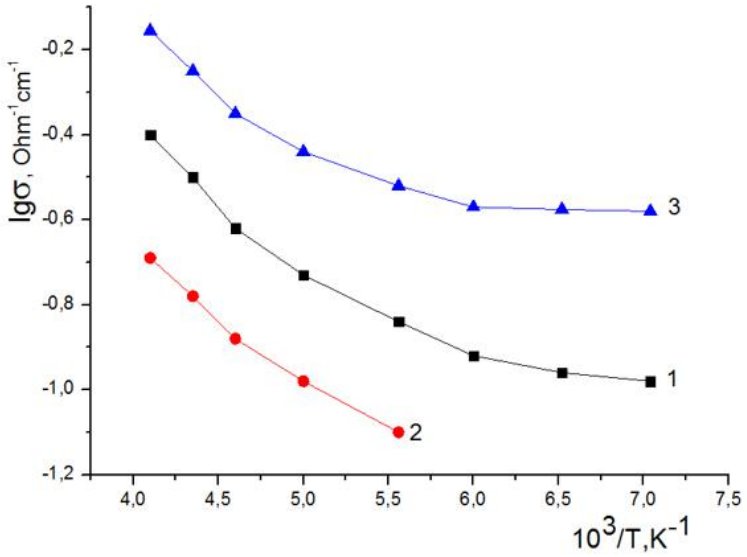

Fig. 1. γ- effect of irradiation on the electrical conductivity of $In_{0.999}Ag_{0.001}Se$ monocrystals: the 1st curve refers to the non-irradiated samples, the 2nd curve to the samples irradiated with a 50 krad dose , and the 3rd curve to the samples irradiated with a 100 krad dose.

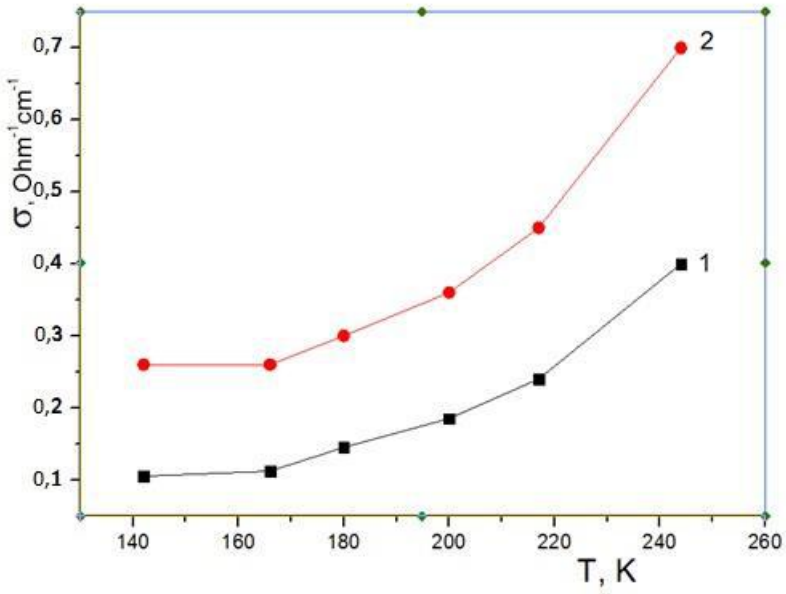

Fig.2. Temperature dependences of electrical conductivity of $In_{0.999}Ag_{0.001}Se$ single crystals: 1 curve refers to non-irradiated samples, 2 curve refers to samples irradiated with a dose of 100 krad.

It can be seen from the figure that the electrical conductivity varies exponentially depending on the temperature, and as the temperature decreases, the difference between the electrical conductivity of unirradiated and irradiated crystals increases. This situation becomes more pronounced when the crystal is irradiated with a dose of 100 krad.

To find the relative change in electrical conductivity, the difference between the electrical

conductivity of the sample irradiated with a dose of 100 krad and the non-irradiated sample was used.

Figure 3 shows the temperature dependence of the relative change of electrical conductivity of non-irradiated and irradiated samples with a dose of 100 krad.

$In_{0.999}Ag_{0.001}Se$ samples with a dose of 100 krad, the difference between the electrical conductivity at appropriate temperatures was determined using the following formula

$$\frac{\sigma_{\gamma-}\sigma_0}{\sigma_0}$$

Here, σ_0 is the electrical conductivity of non-irradiated σ_γ $In_{0.999}Ag_{0.001}$ Se samples irradiated with a dose of 100 krad .

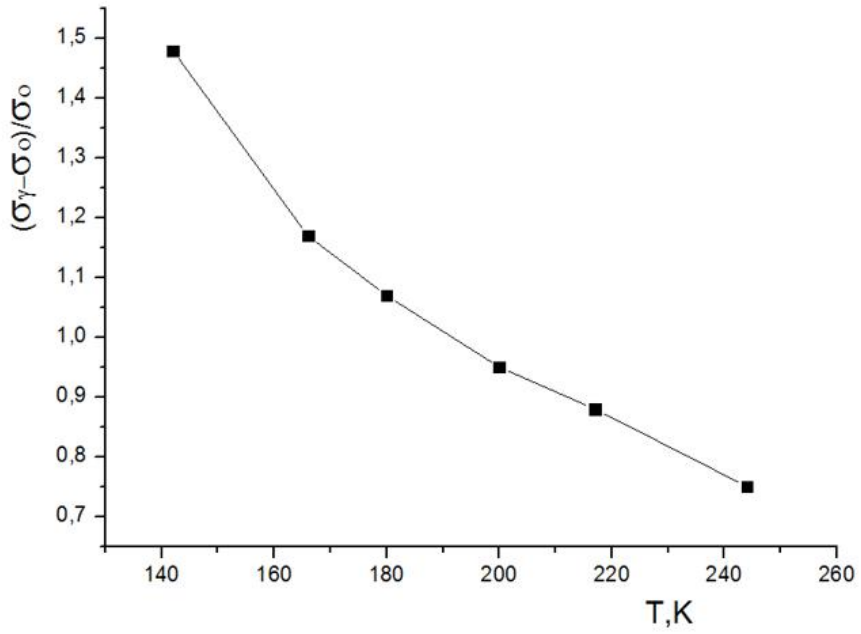

Fig 3 . Temperature dependence of the relative change of electrical conductivities of $In_{0.999}Ag_{0.001}Se$ crystals irradiated with a dose of 100 krad and not irradiated.

RESULTS

It was determined that when $In_{0.999}Ag_{0.001}Se$ crystals are irradiated with g-quanta with a dose of 50 krad, radiation centers with an energy of 0.17 eV appear in the forbidden band and the electrical conductivity decreases. The reason for this is that uncontrolled defects with energy E_v+0.1eV are compensated by defects caused by radiation. As a result of compensation, the concentration of charge carriers decreases. As the radiation dose increases, new centers are not formed, the concentration of previous centers increases. The dependence of the electrical conductivity on the radiation dose occurs with the accumulation of acceptor defects. It was determined that as a result of a dose of 100 krad, the crystals undergo a purification process, which allows the crystals we have studied to be successfully used in various fields of industrial electronics.

[1] *A. Segura, J.P. Geusdon, J.M. Besson, A. Chevy*. Fotovoltaic effect in InSe. Application to solar energy conversion. “Rev. Phys. appl.” 1979, t.14, ¹1, p.253.

[2] *A. Segura, J.P. Geusdon, J.M. Besson, A. Chevy*. Photoconductivity and fotovoltaic effect in in indium selenide. J. Appl. Phys. 1983, t.54, ¹2, p.876

[3] *А.Г. Кязымзаде, А.А. Агаев, В.М. Салманов*. Детекторы оптического излучения на основе слоистых кристаллов GaSe и InSe. ЖТФ, 2007, t.77, c.80-85.

[4] *К.Х. Нагиев, В.М. Салманов*. Оптические модуляторы на основе кристаллов GaSe и InSe. Республиканская научная конференция «Актуальные проблемы физики», посвященная 90-летию БГУ. Баку, 16 мая 2009, с.18.

[5] *Г.Д. Гусейнов, Г.И. Искендеров, Е.М. Керимова*. Взаимодействие мягкого рентгеновского излучения с монокристаллами InSe. Препринт №3, ИФАН, Баку, 1991, 20 с.

[6] *С.Н. Мустафаева, М.М. Асадов, А.А. Исмаилов* Перенос заряда по локализованным состояниям в монокристалле InSe и InSe<Sn>//Физика Низких Температур, 2010, т.36, №4, с.394-397.

[7] *С.Н. Мустафаева, М.М. Асадов, А.А. Исмаилов*. Влияние γ-облучения на параметры локализованных состояний в монокристаллах p-InSe и n-InSe<Sn>//Физика

Низких Температур 2010, т.36, №7, с.805-808.

[8] *А.А. Исмаилов, Ш.Г. Гасымов, Т.С. Мамедов, К.Р. Аллахвердиев*. Влияние давления на электропроводность и эффект холла селенида индия. ФТП, 1992, т.26, в.11, с.1994-1996.

[9] *A.A.Ismailov, N.Z.Gasanov, A.A.Ismailov, Z.M. Nasrullaeva.* Influence of γ-irradiation on the Elektrophysical Properties of $In_{1-x}Sm_xSe$ Single Crystals. American Journal of sosial and Humanitar Research. Global Rearch, Network, vol.3issue, 5-in may 2022, p.120-122.

[10] *A.Ə. İsmayılov, Q.İ. İsaqov, Ə .Ə. İsmayılov.* InSe laylı kristallarında yaranan defektlər Akademik L.M.İmanovun 100 illiyinə həsr olunmuş beynəlxalq konfrans 7 oktyabr 2022, s.141-143.

[11] *E.M. Kerimova, N.Z. Gasanov, A.A. Ismailov.* Electrical and photoelectric properties of solid solutions $In_{1-x}Er_xSe$. GESJ, Physics, 2019, №1(21), p.53-59.

[12] *В.С. Вавилов, Н.П. Кокелидзе, Л.С.Смирнов.* Действие излучений на полупроводники. М., Наука,1988, 191с.

[13] *Г.И. Исаков, А.А. Исмаилов, П.Г. Исмаилова, А.А. Исмаилов, С.С. Абдинбеков, Х.Ш.Велибеков, Т.Я.Оруджев.* Электрические свойства монокристаллов $In_{0.99}Sm_{0.01}Se$ и $In_{0.99}Er_{0.01}Se$ для солнечных элементов. Международный журнал, Альтернативная энергетика и экологии, 2022, №6, с.36-43, Саров.

[14] Конфигурационная модель вещества, под ред. Г.Б. Самсонова, И.Ф. Прядко, Л.Ф. Прядко (Киев, Наук. думка, 1975).

[15] *В.Ю. Ирхин, Ю.П. Ирхин.* Электронная структура, физические свойства и корреляционные эффекты в d–и f-металлах и их соединениях (М., Наука, 2011).

Received: 15.09.2023

ON THE THEORY OF THIRD HARMONIC GENERATION IN A FABRY–PEROT CAVITY

Sh.Sh. AMIROV[1,2], N.V. KERIMLI[1], N.H. GURBANOVA[1], H.A. ABIYEV[1]

[1]*Department of Medical and Biological Physics, Azerbaijan Medical University*
167 S.Vurgun str., Az-1022, Baku, Azerbaijan
[2]*Department of Physics and Electronics, Khazar University, 41 Mahsati str., Az 1096, Baku, Azerbaijan*
Corresponding author :E-mail: phys_med@mail.ru

An analytical expression for the efficiency of conversion into third harmonic in a Fabry-Perot cavity filled with the third order nonlinear medium is obtained in the constant intensity approximation. This approximation takes into account the reverse reaction of excited harmonic wave on the phase of fundamental radiation. It was shown that in order to achieve highest conversion efficiency the optimum values of problem parameters like coefficient of reflection, nonlinear length of medium etc. should be chosen.

Keywords: third harmonic, Fabry-Perot cavity, nonlinear medium, constant intensity approximation.
PACS:78.67. Pt; 42.65-k; 42.62.Hk; 42-70a.

1. INTRODUCTION

Third harmonic generation plays a vital role in optical communications, biological microscopy etc. At Fabry-Perot cavity resonant wavelength in near-infrared regime, the efficiency of THG from a 50 nm thick amorphous GST225 planar film is boosted, by 422 times compared to that of non-resonant conditions [1]. Third harmonic generation in layered or periodically modulated media has been drawing considerable attention [2]. Calculations suggest the possibility of all optical switch at third harmonic frequency controlled by the parameters as intensity and frequency of the fundamental wave [3]. Second harmonic generation occurs at ordered non-centrosymmetric structures that are observed mostly in crystals as wel as metals [4]. Biological materials contain wide-scale non-centrosymmetric buildings with coiled view strucrures and polymeric proteins, for instance, at striated muscle and fibrillar collagen [5]. Generation of third harmonics is due to tripling of the frequency of fundamental wave that means conversion of three photons into one photon of a triplred energy [6]. Third harmonic generation occurs at structural inerfaces, such as local transitions of the refractive index or third-order nonlinear susceptibility [7]. For the Fabry-Perot cavity as wel as V-sahaped cavities authors have derived the rate of conversion of the fundamental frequencies into the second harmonic and the sum frequencies [8]. Third harmonic generation microscopy is a label-free scatter process that is elicited by water-lipid and water protein interfaces, including intra-and extracellular membranes, and extracellular matrix structures [9].

2. THEORETICAL APPROACH AND DISCUSSIONS

In this paper we present the results of analysis of third harmonic generation in the Fabry-Perot cavity filled with medium of third order nonlinear susceptibility. Unlike the constant field approximation , here calculations are carried out in the constant intensity approximation [10] taking into account reverse reaction of generated harmonics on the phase of fundamental. Earlier we have employed this approximation for analysis of frequency conversions in traditional nonlinear crystals [11] as well as metamaterials having negative refractive index in a specific frequency region[12-14].

For the analysis of third harmonic generation in an external cavity we assume that the fundamental wave with frequency ω_1 is normally incident on the nonlinear medium with cubic nonlinearity. As a result of nonlinear interaction between incident wave and nonlinear medium the thir harmonic of frequency $\omega_3 = 3\omega_1$ is generated. The process of generation of third harmonics is described by the following system of truncated equations:

$$\pm\frac{dA_1^{\pm}}{dz} + \delta_1 A_1^{\pm} = -i\gamma_1 A_3^{\pm}(A_1^{\pm})^{*2} e^{\pm i\Delta z}$$
$$\pm\frac{dA_3^{\pm}}{dz} + \delta_3 A_3^{\pm} = -i\gamma_3 (A_1^{\pm})^3 e^{\mp i\Delta z} \quad (1)$$

where $A_1^{\pm}$ and $A_3^{\pm}$ are the complex amplitudes at frequencies ω_1 and $\omega_3 = 3\omega_1$ respectively. Here $\Delta = k_3 - k_2 - k_1$ - is the difference of wave numbers; γ_j - are the nonlinear coupling coefficients; δ_j - are linear absorption coefficients (j=1,2,3). In an external cavity the above set of truncated equations is solved according to the following boundary conditions:

$$A_3^-(l) = R_3 A_3^+(l) e^{-i2k_3 l}\ ;\ A_3^+(0) = R_{30} A_3^-(0)\ ;$$
$$A_1^+(0) = A_{10}\ ;\quad A_1^-(l) = 0 \quad (2)$$

131, H.Javid ave, AZ-1143, Baku
Institute of Physics
E-mail: jophphysics@gmail.com

Here R_{30}, R_3 –are the complex reflective coefficients of third harmonic for the left and right mirrors respectively, when the wave is incident from nonlinear crystal. In the case of consideration fundamental wave freely passes through cavity (R_{10}, = $R_1 = 0$) and third harmonic wave undergo multiple reflections (R_{30}, $R_3 \neq 0$).
Substituting $A_3^{\pm}(z) = a_3^{\pm}(z)e^{[-(\delta_3+3\delta_1+i\Delta)z/2]}$ in above set of equations (1) yiedlds

$$\frac{d^2a_3^{\pm}}{dz^2} + \mu^2 a_3^{\pm} = 0 \tag{3}$$

where $\mu = \left[3\Gamma_3^2 + \left(\frac{\delta_3-3\delta_1-i\Delta}{2}\right)^2\right]^{1/2}$
Solving the equation (3) for the complex amplitude of third harfmonic in the constant intensity approximation gives :

$$A_3^+(l) = \frac{-i\gamma_3 A_{10}^2 l sinc\mu l \cdot e^{[-(\delta_3+3\delta_1+i\Delta)l/2]}}{1-r_{30}r_3 K \cdot e^{[-\frac{(\delta_3+3\delta_1)l+i(\varphi+2k_3l+\Delta l)}{2}]}} \tag{4}$$

where $K = cos\mu l + [(\delta_3 + 3\delta_1 + i\Delta)/2\mu]sin\mu l$, $\Gamma_3^2 = \gamma_1\gamma_3 I_{10}^2$, $r_{30}, r_3 -$ are absolute values of coefficients of reflection and $\varphi = \varphi_{30} + \varphi_3$ are the phase shifts for harmonic wave at mirrors.
From (4) we get expression for the intensity of third harmonics at the output mirror ($r_{30} = 1$) :

$$I_3^+(l) = \frac{\gamma_3^2 I_{10}^3 \chi^{-1}(sin^2 xch^2 y + sh^2 y cos^2 x)exp[-(\delta_3+3\delta_1)l]}{1-2r_3\chi_1 cos\Psi exp[-(\delta_3+3\delta_1)l/2]+r_3^2\chi_1^2 \cdot exp[-(\delta_3+3\delta_1)l]} \tag{5}$$

here $x = \chi^{1/2} l cos\theta/2$, $y = \chi^{1/2} l sin\theta/2$, $\chi = \left[3\Gamma^2 + \frac{\Delta^2}{4} - \frac{(\delta_3-3\delta_1)^2}{4}\right]^2 +$
$+ \frac{\Delta^2(\delta_3-3\delta_1)^2}{4}$; $\theta = arctg\left[\frac{\Delta(\delta_3-3\delta_1)/4}{3\Gamma^2+\frac{\Delta^2}{4}-\frac{(\delta_3-3\delta_1)^2}{4}}\right]$;

$$\chi_1^2 = (cosxchy + asinxchy - bcosxchy)^2 + (bsinxchy + acosxshy - sinxshy)^2$$

$a = \frac{\Delta y+(\delta_3+3\delta_1)x}{2(x^2+y^2)} l$; $b = \frac{\Delta x-(\delta_3-3\delta_1)y}{2(x^2+y^2)} l$, $\Psi = \varphi + 2k_3 l + \frac{\Delta l}{2} - \theta_1$

$$\theta_1 = arctg\frac{bsinxchy + acosxshy - sinxchy}{cosxchy + asinxchy - bcosxshy}$$

From the obtained expression for the intensity of third harmonics we can get efficiency of frequency conversion into third harmonic: $\eta = I_{3,out.}^+/I_{10}$

$$\eta = \frac{\gamma_3^2 I_0^2 \chi^{-2}(sin^2 x + sh^2 y)exp[-(\delta_3+3\delta_1)l]}{1-2r_3\chi_1 cos\Psi exp[-(\delta_3+3\delta_1)l/2]+r_3^2\chi_1^2 \cdot exp[-(\delta_3+3\delta_1)l]} \tag{6}$$

where $I_{3,out.}^+ = I_3^+(l)(1 - r_3^2)$
When $r_3 = 0$ from the formula (6) we obtain

$$\eta_0 = \gamma_3^2 I_0^2 \chi^{-2}(sin^2 x + sh^2 y)exp[-(\delta_3 + 3\delta_1)l] \tag{7}$$

Using last two formulas gives us gain ($\tilde{\eta} = \eta/\eta_0$) due to use the resonator

$$\tilde{\eta} = \frac{(1-r_3^2)}{1-2r_3\chi_1 cos\Psi exp[-(\delta_3+3\delta_1)l/2]+r_3^2\chi_1^2 \cdot exp[-(\delta_3+3\delta_1)l]} \tag{8}$$

As can be seen from above expression one of the ways ofto acheive the maximum gain is fulfilling the resonance phase condition ($\Psi = 2n\pi$):

$$\varphi + 2k_3 l + \frac{\Delta l}{2} - \theta = 2n\pi \tag{9}$$

Thus in the constant intensity approximation resonance phase condition depends on the pump intensity. At definite values of other parameters of problem condition $\tilde{\eta} > 1$ implies limitation to the absolute value of coefficient of reflection r_3 of harmonic wave: $r_3 < 2\mu cos\,\Psi/(1+\mu^2)$. Other condition for obtaining maximum frequency conversion serves choosing optimum value of reflective coefficient.

Theoretical analysis showed that the gain due to use of cavity has pronounced maxima depending on the coefficient of reflection r_3 and reduced length of nonlinear crystal has pronounced maxima. Gain reaches its maxima at optimum values of coefficient of reflection depending on other parameters of problem. Also it was found that in order to obtain effective frequency conversion it is reasonable to choose optimum length of nonlinear crystal. Optimum length of crystal decreases with increase in difference of wave numbers of interacting waves.

3. CONCLUSIONS

On the basis of above stated one can conclude that resonance phase condition determines the effective frequency conversion in third order nonlinear medium. This condition is a function of intensiy of fundamental wave. When reflective coefficient does no agree with inequality obtained in this paper the employment of resonator is not reasonable. An optimum value of coefficient of reflection depends on nonlinear length of medium, intensity of pump wave , phase mismatch etc.

[1] *C. Tun, L. Kuan, T. Yutao* et al. Giant enhancement of third harmonic generation from based Fabry-Perot cavity. Archiv, 2019, physics,1901.08795.

[2] *N. Hashizume, M. Ohashi, R. Ito* Opical harmonic generation in multilayered structures: a comprenhensive analysis. J. Opt. Soc. Am., 1995, B12, pp.1894-1904.

[3] *J. Jose, S.D. Gupta* . Third harmonic generation in layered media in presence of optical bistability of the fundamental. Pramana, journal of Physics, 1998, v. 50, No.3, pp.239-251]

[4] *S.Y. Chen, C.Y. Chen, and C.K. Sun.* Epi-third and second harmonic generation microscopic imaging of abnormal enamel. Opt.Express, 2008, v.16, pp. 11670-11679.

[5] *P. Campagnola, A. Millard, M. Terasaki M.* Three dimensional high resolution second-harmonic generation imaging of endogeneous structural proteins in biological tissues. Biophysics 2002, J.82483-50. https.//doi.org/10.1016/50006-3495(02)75414-3 2002.

[6] *Y. Barad, H. Eisenberg, M. Horowitz, and Y. Silberberg.* Nonlinear scanning laser microscopy by third harmonic generation. Appl.Phys. Lett., 1997, 70, pp.922-931.

[7] *M. Muller, J. Squier, K. Wilson, and G. Brakenhoff G.* 3D microscopy ofd transparent objects using third-harmonic generation. J. Microscopy,1998, v.191, pp.266-274.

[8] *L. Fri , P. Mandel, E. Viktorov* . Intracavity second harmonic generation in a Fabry-Perot resonator: Polarization effects.Quantum and Semiclassical optics: Joiurnal of the European optical Society,1998, part B, v.10, No.1, pp.1355-1363.

[9] *B. Weigelin, G.J. Bakker and P. Friedl.* Third harmonic generation microscopy of cells and tissue organization. Journal of Cell Science, 2016, v. 1 No. 11, pp.32-43.

[10] *Z.H. Tagiev, A.S. Chirkin*. Fixed intensity approximation in the theory of nonlinear waves Zh.Eksp. Teor. Fiz.1977, 73, pp.1271-1282.

[11] *Sh.Sh. Amirov, Z.H. Tagiyev*. Conversion of frequencies of ultrashort pulses in external cavity. Optics and Spectroscopy, v.69, No. 3. pp.678-686.

[12] *R.J. Kasumova, Sh.Sh. Amirov*. Nonstationary sum frequency generation in inhomogeneous optical fiber. AJP "Fizika"(EN), 2022, Vol.XXVIII, No. 2, p.24-30.

[13] *R.J. Kasumova, Sh.Sh. Amirov, Sh.A. Shamilova.* Parametric ineraction of optical waves in metamaterials under low-frequency pumping. Quantum Electronics.2017. v.47, No.7,pp.655-660.

[14] *R.J. Kasumova, Z.H. Tagiev, Sh.Sh. Amirov, Sh.A. Shamilova, G.A. Safarova*. Phase effects at parametrical interaction in metamaterials. Journal of Russian Laser Research. 2017. V.38.p.211-218.

Received: 19.09.2023

ISSN 1028-8546

2023, Vol. XXIX, №3
Section: En

CONTENTS